



HAL
open science

Evidence of a Transient Aseismic Slip Driving the 2017 Valparaiso Earthquake Sequence, From Foreshocks to Aftershocks

Luc Moutote, Yuji Itoh, Olivier Lengliné, Zacharie Duputel, Anne Socquet

► **To cite this version:**

Luc Moutote, Yuji Itoh, Olivier Lengliné, Zacharie Duputel, Anne Socquet. Evidence of a Transient Aseismic Slip Driving the 2017 Valparaiso Earthquake Sequence, From Foreshocks to Aftershocks. *Journal of Geophysical Research: Solid Earth*, 2023, 128 (9), 10.1029/2023JB026603 . hal-04240117

HAL Id: hal-04240117

<https://hal.science/hal-04240117>

Submitted on 13 Oct 2023

HAL is a multi-disciplinary open access archive for the deposit and dissemination of scientific research documents, whether they are published or not. The documents may come from teaching and research institutions in France or abroad, or from public or private research centers.

L'archive ouverte pluridisciplinaire **HAL**, est destinée au dépôt et à la diffusion de documents scientifiques de niveau recherche, publiés ou non, émanant des établissements d'enseignement et de recherche français ou étrangers, des laboratoires publics ou privés.

JGR Solid Earth



RESEARCH ARTICLE

10.1029/2023JB026603

Evidence of a Transient Aseismic Slip Driving the 2017 Valparaiso Earthquake Sequence, From Foreshocks to Aftershocks

Luc Moutote¹ , Yuji Itoh^{2,3} , Olivier Lengliné¹ , Zacharie Duputel⁴ , and Anne Socquet² 

¹Institut Terre et Environnement de Strasbourg, Université de Strasbourg/EOST, CNRS, Strasbourg, France, ²University of Grenoble Alpes, University of Savoie Mont Blanc, CNRS, IRD, University of Gustave Eiffel, ISTerre, Grenoble, France, ³Earthquake Research Institute, The University of Tokyo, Tokyo, Japan, ⁴Observatoire Volcanologique du Piton de la Fournaise, Université Paris Cité, Institut de Physique du Globe de Paris, CNRS, Paris, France

Key Points:

- We use a high resolution seismic catalog and GPS to investigate seismic and aseismic process before and after the Valparaiso mainshock
- An unusually high seismicity and a slow slip event is continuously observed from the foreshock sequence up to days after the mainshock
- Rather than a nucleation phase of the mainshock, the slow slip event acts as an aseismic loading of nearby faults during the entire sequence

Supporting Information:

Supporting Information may be found in the online version of this article.

Correspondence to:

L. Moutote,
lmoutote@unistra.fr

Citation:

Moutote, L., Itoh, Y., Lengliné, O., Duputel, Z., & Socquet, A. (2023). Evidence of a transient aseismic slip driving the 2017 Valparaiso earthquake sequence, from foreshocks to aftershocks. *Journal of Geophysical Research: Solid Earth*, 128, e2023JB026603. <https://doi.org/10.1029/2023JB026603>

Received 27 FEB 2023

Accepted 12 SEP 2023

Author Contributions:

Conceptualization: Luc Moutote, Yuji Itoh, Olivier Lengliné, Zacharie Duputel, Anne Socquet

Data curation: Luc Moutote, Yuji Itoh, Olivier Lengliné

Formal analysis: Luc Moutote, Yuji Itoh, Olivier Lengliné

Funding acquisition: Zacharie Duputel, Anne Socquet

Methodology: Luc Moutote, Yuji Itoh, Olivier Lengliné, Zacharie Duputel, Anne Socquet

Abstract Following laboratory experiments and friction theory, slow slip events and seismicity rate accelerations observed before mainshocks are sometimes interpreted as evidence of a nucleation phase. However, such precursory observations still remain scarce and are associated with different time and length scales, raising doubts about their actual preparatory nature. We study the 2017 Valparaiso $M_w = 6.9$ earthquake, which was preceded by aseismic slip accompanied by an intense seismicity, suspected to reflect its nucleation phase. We complement previous observations, which have focused only on precursory activity, with a continuous investigation of seismic and aseismic processes from the foreshock sequence to the post-mainshock phase. By building a high-resolution earthquake catalog and searching for anomalous seismicity rate increases compared to aftershock triggering models, we highlight an over-productive seismicity starting within the foreshock sequence and persisting several days after the mainshock. Using repeating earthquakes and high-rate GPS observations, we highlight a transient aseismic perturbation starting 1-day before the first foreshock and continuing after the mainshock. The estimated slip rate over time is lightly impacted by large magnitude earthquakes and does not accelerate toward the mainshock. Therefore, the unusual seismic and aseismic activity observed during the 2017 Valparaiso sequence might be interpreted as the result of a slow slip event starting before the mainshock and continuing beyond it. Rather than pointing to a possible nucleation phase of the 2017 Valparaiso mainshock, the identified slow slip event acts as an aseismic loading of nearby faults, increasing the seismic activity, and thus the likelihood of a large rupture.

Plain Language Summary Both laboratory experiments and friction theory show that earthquakes do not begin abruptly but are preceded by an accelerating slip associated with a seismicity increase. On the field, however, such precursory observations still remain scarce and are associated with different characteristic time and length scales, raising doubts that they actually reflect the same nucleation phenomena. We study the 2017 Valparaiso $M = 6.9$ earthquake, which was preceded by both a slow slip and an intense seismicity suspected to reflect such nucleation phase. We complement previous studies, that have focused only on precursory activity, with a continuous investigation of seismic and slow slip before and after the mainshock. Using refined earthquake detection tools, we highlight a seismicity excess starting before and persisting several days after the mainshock. Using repeating earthquakes and high-resolution GPS, we show that the slow slip does not accelerate toward the mainshock, but continues after it. Therefore, rather than pointing to a possible accelerating nucleation phase of the Valparaiso mainshock, we suggest that the slow slip drives an enhanced seismic activity that is not mainshock-directed. Within such slow-slip driven seismicity, the probability of triggering a large earthquake (subsequently considered as the mainshock) is increased.

1. Introduction

Both laboratory experiments and friction theory show that earthquake ruptures do not begin abruptly but are preceded by a slow slip phase accelerating over a finite nucleation zone (Das & Scholz, 1981; Dieterich, 1992; Latour et al., 2013; McLaskey, 2019; Rubin & Ampuero, 2005). However, extrapolating the results of these models to natural faults is not straightforward, as some parameters entering the model definition are not known for large-scale systems (Ampuero & Rubin, 2008; Kaneko & Ampuero, 2011). In particular, the size of the nucleation zone predicted by such models is not well constrained. If the nucleation length is large, the slow,

© 2023. The Authors.

This is an open access article under the terms of the [Creative Commons Attribution-NonCommercial License](https://creativecommons.org/licenses/by/4.0/), which permits use, distribution and reproduction in any medium, provided the original work is properly cited and is not used for commercial purposes.

Supervision: Olivier Lengliné, Zacharie Duputel, Anne Socquet

Validation: Luc Moutote, Yuji Itoh, Olivier Lengliné, Zacharie Duputel, Anne Socquet

Visualization: Luc Moutote, Yuji Itoh

Writing – original draft: Luc Moutote, Yuji Itoh, Olivier Lengliné

Writing – review & editing: Luc Moutote, Yuji Itoh, Olivier Lengliné, Zacharie Duputel, Anne Socquet

quasi-static, predicted crack-like expansion could be observed on natural faults. On the other hand, an accelerating pulse in a small nucleation zone could be more difficult to detect in practice. The existence and detectability of such nucleation phases before actual earthquakes is thus an important question with direct implications for earthquake prediction and seismic hazard assessment (Brodsky & Lay, 2014).

Recently, with geodetic measurements, several aseismic slip transients (also called slow slip events) have been reported before the occurrence of large earthquakes (Durand et al., 2020; Marill et al., 2021; Mavrommatis et al., 2014; Ruiz et al., 2014, 2017; Socquet et al., 2017; Voss et al., 2018). In addition to geodetic observations, other observations such as repeating earthquakes are frequently used to support the detection of these aseismic processes (Igarashi et al., 2003; Kato et al., 2012, 2016; Mavrommatis et al., 2015; Nadeau & Johnson, 1998; Uchida, 2019). Because of their timing, preceding large events, these transient aseismic slips are sometimes interpreted as an evidence of the mainshock nucleation phase as depicted by theory and laboratory experiments. However, despite the densification of geodetic and seismic networks around active faults, precursory aseismic slip observations still remain scarce in comparison with the number of instrumentally recorded large earthquakes. The reported examples often have large uncertainties in both their location and temporal evolution, making it difficult to infer any acceleration trend as the mainshock approaches. Moreover, there are significant discrepancies in the duration of reported preparatory slip, ranging from a few tens of seconds (Tape et al., 2018) to decades before the main rupture (e.g., Marill et al., 2021; Mavrommatis et al., 2014). While these different durations could potentially reflect differences in nucleation zone size or frictional parameters, they also raise doubts about whether these observations are actually reflecting the same unique geophysical process.

On the other hand, many large earthquakes are also preceded by seismicity rate increases, which may be additional evidence of a slow preparatory process before large earthquakes (Bouchon et al., 2011, 2013; Dodge et al., 1995, 1996; Seif et al., 2019). In the framework of a slow nucleation phase, such foreshock activity is interpreted as rupture of locked small asperities driven by background aseismic slip acceleration (Dodge et al., 1996; McLaskey, 2019; Ohnaka, 1992). However, analyzing solely the seismicity rate to infer preparatory process before large earthquake is a difficult task (Ross et al., 2019; van den Ende & Ampuero, 2020; Moutote et al., 2021). Indeed, earthquakes are strongly spatiotemporally clustered (Helmstetter & Sornette, 2003; Marsan & Lengline, 2008), mainly because they interact with each other, making their probability of occurrence dependent on the past seismic activity. Therefore, the successive occurrence of earthquakes and their interactions can lead to seismicity rate increases, even without any external loading process (Felzer et al., 2004; Helmstetter & Sornette, 2003; Marsan & Enescu, 2012). Therefore, determining if the rise of foreshock earthquake sequence results uniquely from earthquake interactions or could in some occasion represent a true signal associated with an underlying aseismic transient remains actively debated (Ellsworth & Bulut, 2018; Gombert, 2018; Kato et al., 2016; Llenos et al., 2009; Mignan, 2015; Tape et al., 2018).

It is worth mentioning that detecting both a transient aseismic slip and an enhanced earthquake activity before large earthquakes may not appear as sufficient evidence of nucleation phase. There are indeed multiple evidence of earthquake swarms that have been linked to a slow slip transient without culminating into a large rupture (Lohman & McGuire, 2007; Nishikawa et al., 2021; Vallée et al., 2013) and we know that transient aseismic slip can occur independently from any significant seismicity (Radiguet et al., 2012; Rogers & Dragert, 2003). The observation of transient aseismic slip before large earthquakes is also sometimes shown to rather be independent fault process that happen to trigger subsequent large earthquakes by stress transfer (Klein et al., 2018, 2021, 2023; Radiguet et al., 2016; Voss et al., 2018). An interesting example was reported near the Guerrero gap, Mexico, where at least four episodic and co-located slow slip events have been successively detected over 10 years without being followed by any significant earthquake. Yet, in 2014, a slow slip event on the same portion of the interface was followed by the $M_w = 7.3$ Papanaoa earthquake (Radiguet et al., 2016). Such an example shows that detecting both a transient aseismic slip and an unusually high seismicity before a large earthquake may not necessarily represent a deterministic nucleation process of a mainshock. Therefore, questions subsist on the interpretation of the seismic and aseismic processes observed before large earthquakes and on the estimation of their predictive power for the subsequent large rupture.

In this study, we analyze in detail seismic and aseismic processes before and after the April 2017 Valparaiso $M_w = 6.9$ earthquake (Chile; Figure 1). This mainshock was preceded by an intense 2-day long foreshock sequence with magnitudes up to $M_w = 6$ and was followed by an abundant aftershock activity. In addition, an aseismic precursory fault slip has been reported during the foreshock sequence (Caballero et al., 2021; Ruiz et al., 2017).

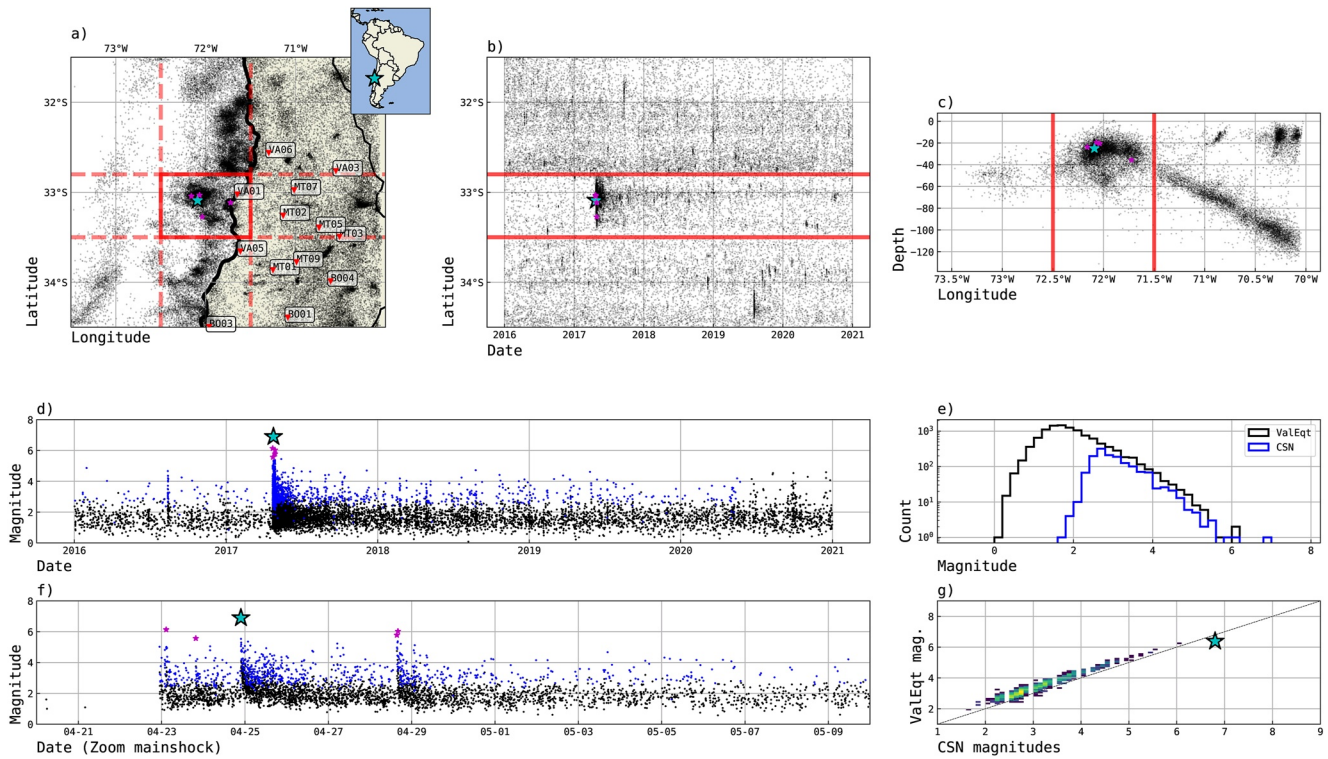


Figure 1. Time, location and magnitude of earthquakes detected in this study between 2016 and 2021. (a) Horizontal location of earthquakes. The thick red line shows the extent of the ValEqt catalog analyzed in this study. The red triangles show the location of the 13 broadband stations used to build the catalog. (b) Time evolution of the latitude of earthquakes between the two vertical red-dashed lines in panel (a). (c) Depth and longitude of earthquakes between the two horizontal red-dashed lines in panel (a). Magenta stars indicate $M \geq 6$ earthquakes. (d) Time and magnitude of earthquakes within the ValEqt sub-region (thick red rectangle in panel (a)). Black dots are our catalog. Blue dots (in the foreground) are the Centro Seismológico Nacional (CSN) catalog used as reference. (e) Gutenberg-Richter magnitude frequency distribution of our ValEqt (blue) and CSN (blue) catalogs. (f) Same as (d) but zoomed in time in the vicinity of the mainshock. (g) Comparison of magnitude estimations for common earthquakes in the CSN and the ValEqt catalogs. The light blue star indicates the $M_w = 6.9$ mainshock.

This aseismic pre-slip may have initiated before the first foreshock and persisted, at least, up to the mainshock (Caballero et al., 2021). However, its onset timing and detailed time evolution are still unclear due to the sampling intervals of the GPS data previously used (6 hr and 1 day in Ruiz et al. (2017) and Caballero et al. (2021), respectively). Furthermore, aseismic processes following the mainshock have not been investigated. The seismicity rate during the foreshock-mainshock-aftershock sequence was not yet tested against earthquake interaction model to confirm previously suggested unusual increases. Hence, we, first, build a high-resolution seismic catalog from 2016 to 2021. Then, we compare the seismicity in the vicinity of the mainshock with aftershock triggering models to highlight unusual variations in seismicity rates. In the second part, we investigate the aseismic slip transient during the entire earthquake sequence using repeating earthquake and high-rate GPS observation. We, finally, discuss whether the aseismic slip transient is part of the nucleation of the mainshock or it just mediates the whole Valparaiso seismic sequence.

2. ValEqt: A High Resolution Catalog

In order to carry out a detailed analysis of the micro-seismic activity near the mainshock, we build a high resolution catalog using recently developed detection methods. We use 13 broadband stations from the National Seismological Center (CSN) of the University of Chile (Barrientos & National Seismological Center (CSN) Team, 2018) in the vicinity of the mainshock from 1 January 2016 to 1 January 2021 (see Figure 1). Only a few stations were available earlier than 2016, which does not allow us to carry out a reliable seismicity analysis before that date.

2.1. Detection, Location and Magnitude Estimation

We pick P- and S wave arrivals of earthquakes on daily raw waveforms using EQTransformer, an automatic deep learning phase picker trained on a worldwide earthquake database (Mousavi et al., 2020a). We associate phases

picks into events with REAL (Zhang et al., 2019a), performed over a 3° by 3° grid. We only consider events for which both P and S phases are associated on at least three stations. We locate events using NonLinLoc (Lomax et al., 2000) in a 3D velocity model of Chile (Ruiz et al., 2017). We discard events with a NonLinLoc root mean square residual (RMS) above 1 s to avoid false detections.

We then estimate a local magnitude following the original Richter approach on Wood-Anderson seismometers. For that purpose, we correct the recorded waveforms from their instrument response and convolve them with a Wood-Anderson response. For all stations and horizontal components, we convert the maximum zero to peak S waves amplitude, A_{WA} , into a magnitude, M , using the Richter empirical formula (Richter, 1935, 1958; Shearer, 2019):

$$M = \log_{10}(A_{WA}) - 2.21 + 2.56\log_{10}(\Delta) \quad (1)$$

where A_{WA} , is in mm and Δ is the hypocentral distance in km. The event magnitude is taken as the median of all estimations over stations/components. Given its proximity to the ocean, the Valparaiso region is prone to oceanic microseismic noise that dominates the S wave amplitude of small events. To reduce the noise level, we thus first filter all waveforms between 1 and 20 Hz prior to the magnitude estimation. If an event is estimated with a magnitude $M > 3$, we re-estimate its magnitude accounting for lower frequencies with a 0.05–20 Hz bandpass filtering.

The resultant catalog consists of more than 75,000 events from 2016 to 2021 within a 3 by 3° region centered on the Valparaiso mainshock. Over the same region and period, the official Chilean catalog (Centro Seismologico Nacional, CSN) reported only ~7,000 events. Figure 1 shows the spatial and temporal distribution of earthquakes according to this catalog.

2.2. Event Selection and Comparison With the CSN Catalog

To study the seismic activity in the vicinity of the mainshock, we extract all the earthquakes in a sub-region within $-33.5^\circ \leq \text{Latitude} \leq -32.8^\circ$ and $-72.5^\circ \leq \text{Longitude} \leq -71.5^\circ$ with no depth cutoff (Plain red rectangle in Figure 1a). This sub-catalog (hereafter, referred to ValEqt catalog) gathers more than 10,000 events. Our goal here is to focus on seismicity in the vicinity of the mainshock that is not affected by other nearby large earthquakes. From Figure 1b we see several temporally clustered seismic activity. The largest one related to the 2017 $M_w = 6.9$ Valparaiso mainshock. We see that none of the earthquakes outside our selection range seems to significantly affect the seismic activity within the sub-region. The depth distribution of earthquakes along longitude clearly highlights the subduction surface (Figure 1c). The 2017 activity is located on the shallowest part of the subduction surface with no direct connection with deeper activities.

We compare our ValEqt catalog with the CSN catalog (Figures 1d and 1f) in the same sub-region. The Gutenberg-Richter distribution in Figure 1e shows that the ValEqt catalog includes much more small magnitude earthquakes than the CSN catalog, lowering the local magnitude of completeness from $M_c^{CSN} = 3$ to $M_c^{ValEqt} = 2$. Our detection procedure identified almost all earthquakes on CSN catalog. We only miss 12 CSN earthquakes all with a magnitude below three, either because the data of the 13 stations used in our study were unavailable at that time or these earthquakes were interlaced with the waveform of a preceding earthquake, making it difficult to pick their P and S phases even after a careful review. On the other hand, thanks to EQTransformer, we detected many earthquakes with a magnitude above three not listed in CSN catalog. These newly identified earthquakes mainly occurred immediately after a larger earthquake, making them difficult to detect by standard methods (i.e., STA/LTA or visual inspection) because of the amplitude ratio. Figure 1g shows the differences in magnitude for earthquakes recorded in both catalogs. Overall, the ValEqt magnitudes are consistent with the CSN estimations, but with a constant bias of about +0.2 units. This shift could result from the use of a different relation to compute earthquakes magnitude between both catalogs. Because local magnitude saturates for large magnitude earthquakes, the mainshock magnitude was originally underestimated as $M = 6.2$ by our procedure. We, therefore, fix manually its value based on its moment magnitude $M_w = 6.9$. Locations from the ValEqt catalog are similar to those reported by CSN (see Figure S1 in Supporting Information S1). Latitude, longitude and depth $1 - \sigma$ uncertainties are estimated to 0.02° , 0.06° and 6.3 km, respectively. The larger uncertainties in longitude are likely due to the offshore locations of earthquakes constrained by only onland stations. From Figure 1c, we see that earthquakes within the sub-region are widely dispersed at depth, with events sometimes located below the subduction interface. Events at large depth are associated with a small number of phase picks, resulting in a large depth uncertainty (see Figures S2 and S3 in Supporting Information S1). The mainshock and other $M_w > 4$

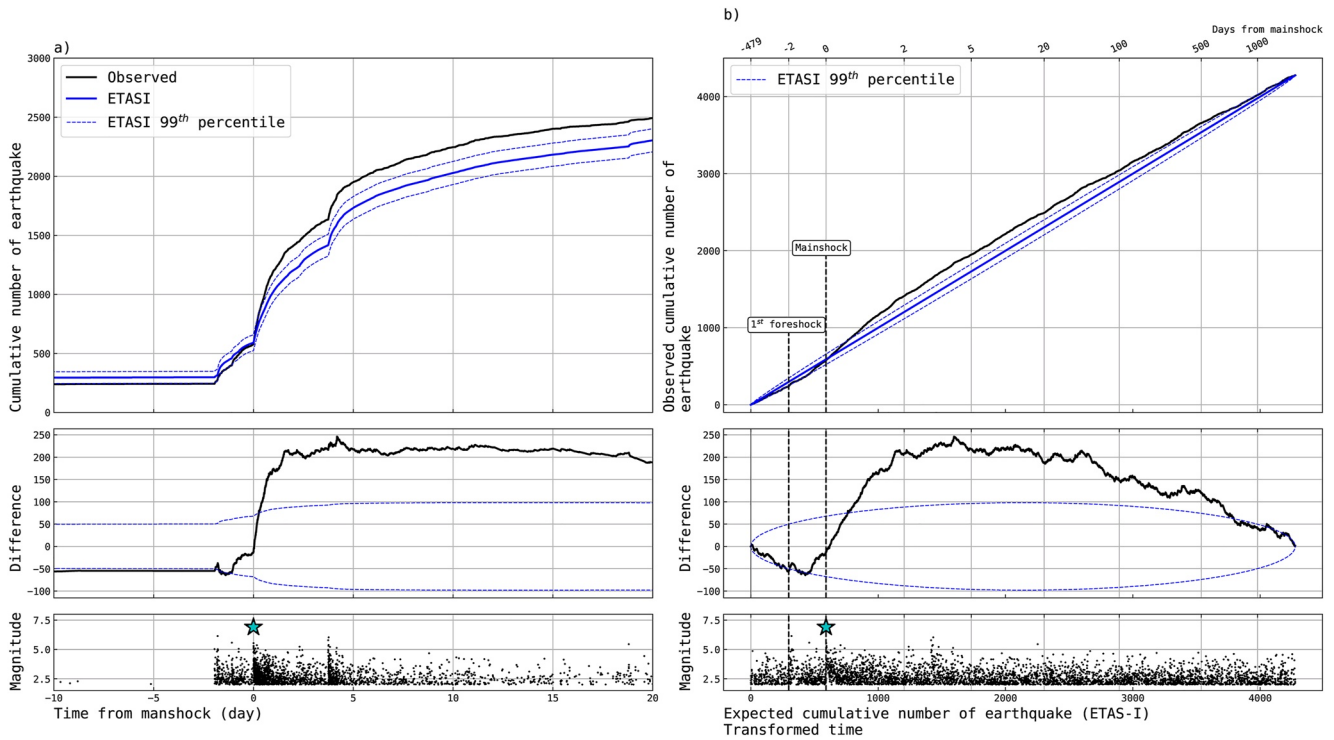


Figure 2. (a) Time-evolution of the cumulative number of earthquakes observed in the ValEqt catalog (black) and predicted by the best fitting ETASI model (blue) around the mainshock time. The blue dotted line shows the ETASI 99th percentile confidence interval. The middle subplot is the difference between the blue and black lines. Black dots in the bottom subplot indicate the time-magnitude evolution of the ValEqt catalog. (b) Same as (a) but for the full 5-years period and with the transformed-time domain axis (Ogata, 1988). The blue star indicates the mainshock. Note how the transformed time domain allows an efficient analysis of the full 5-yr seismicity with respect to the ETASI model.

earthquakes in the region are most likely located on the megathrust interface according to their location and shallow thrusting mechanism (Caballero et al., 2021). Given the large depth uncertainties, it is thus reasonable to assume that most seismic events in the area are located on the subduction interface.

3. Seismicity Analysis

The high resolution ValEqt catalog allows us to obtain a refined view of the seismicity rate variations observed in the region before and after the $M_w = 6.9$ Valparaiso mainshock. The two largest foreshocks are recorded with $M = 6.1$ and $M = 5.5$, approximately 2 and 1 days before the mainshock, respectively. The largest aftershock occurred 4 days after the mainshock with a magnitude $M = 6.1$.

Because of its space and time correlation with the mainshock, a previously reported slow slip event during the foreshock sequence (Caballero et al., 2021; Ruiz et al., 2017) is suspected to reflect the nucleation process of the $M_w = 6.9$ earthquake and may possibly drive part of the foreshock seismicity. However, sharp increase of the seismicity rate following the two largest foreshocks in Figure 2a suggests that a large part of the seismicity may be explained only by aftershock triggering and do not require any slow-slip as their background driver. Therefore, we test the hypothesis that the detected seismicity can be explained by models that account only for earthquake interactions. We use two temporal models of aftershock triggering: the Epidemic Type Aftershock Sequence (ETAS) model (Ogata, 1988; Zhuang et al., 2012) and a model-independent stochastic declustering (MISD) approach (Marsan & Lengline, 2008). We ignore the spatial variation of seismicity and focus only on its temporal variations because the studied region is sufficiently small and isolated from any seismicity rate variations from surrounding regions.

3.1. ETAS and Short-Term Incompleteness

The ETAS model has been widely used to generate synthetic earthquake catalogs (Zhuang & Touati, 2015). It can serve as a basis for establishing a reference earthquake catalog and testing any deviation from it (Marsan et al., 2014; Moutote et al., 2021; Ogata, 1989, 1992; Seif et al., 2019). It is also used to forecast seismicity

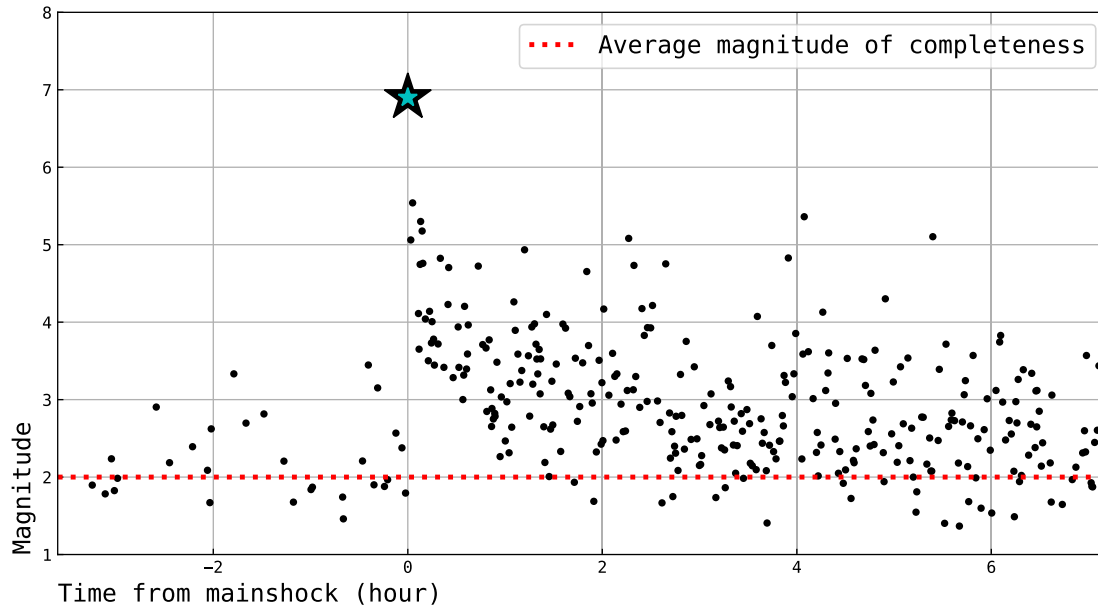


Figure 3. Short-term incompleteness after the Valparaiso mainshock. The red horizontal line is the average magnitude of completeness (M_c) estimated from the Gutenberg-Richter's law distribution of the entire ValEqt catalog. Note the lack of low magnitude earthquakes above M_c during the earliest aftershock times. The light blue star indicate the mainshock.

(Taroni et al., 2018; Zhuang, 2012). The ETAS model is a superposition of a stationary background seismicity term and an aftershock triggering scaled in intensity by the magnitude of the triggering event. The conditional intensity $\lambda_0(t)$ (i.e., the expected seismicity rate at t) given by the ETAS model can be written as:

$$\lambda_0(t) = \mu + \sum_{i|t_i < t} A e^{\alpha(M_i - M_c)} (t - t_i + c)^{-p}, \quad (2)$$

where μ is the stationary background seismicity rate. The sum on the right hand side of this equation describes the expected aftershock seismicity rate at time t , triggered by all the preceding events. The parameters c and p describe the time-decay in the aftershock seismicity rate (Omori, 1895; Utsu et al., 1995). The intensity of the triggering is scaled by A and α , the global aftershock productivity of the region and the magnitude dependency in the number of triggered events, respectively. M_c is the magnitude of completeness of the catalog. In the ETAS model, magnitudes are assumed to be independent and distribute according to Gutenberg-Richter's law (G-R). We can write the G-R probability density function as:

$$f_0(M) = \beta e^{-\beta(M - M_c)}, \quad (3)$$

$\beta = b \ln(10)$ with b the b-value of the G-R law. The G-R law and the ETAS model are only defined above the magnitude of completeness M_c that is supposed to be constant over time. However, in actual seismicity catalogs, we frequently observe temporal variations of M_c (de Arcangelis et al., 2018; Hainzl, 2016; Kagan, 2004). Such variations of M_c are usually attributed to deterioration of the detection performance of low magnitude earthquakes during network maintenance or during period of high seismic activity. The latter is our main concern for the ValEqt catalog since the data availability is quite constant over the studied time-period. When the seismicity rate is high, records of seismic wave of low magnitude earthquakes are likely to be hidden by larger magnitude events. As shown in Figure 1e, we estimate an average magnitude of completeness $M_c = 2$ for the ValEqt catalog over 5 years. However, M_c can increase just after large earthquakes because of the numerous aftershocks they trigger. Figure 3 shows a deficiency in small magnitude earthquakes in the first hour following the $M_w = 6.9$ mainshock and the magnitude of completeness rose up to $M_c \sim 3.5$ immediately after it. The observed $M \geq 2$ earthquake rate is, therefore, underestimated just after the mainshock, which may bias the estimation of an ETAS magnitude-dependent triggering process. This bias is often referred to as Short-Term Incompleteness because it is visible just after large earthquakes (de Arcangelis et al., 2018; Hainzl, 2016; Kagan, 2004). However, it can be generalized to a Rate-dependent incompleteness (Hainzl, 2021) since missing low magnitude events can affect any time-window with a sufficiently high seismicity rate.

Table 1
Best Fitting ETASI Parameters Extracted From the ValEq Catalog

Parameter	A	c (Minutes)	p	$\alpha = \beta$	μ (events/ day)	T_b (seconds)
Value	$9.9e - 3$	11.74	1.18	1.71	0.27	116.57

To accommodate our seismicity analysis with $M_c = 2$ while taking into account the rate-dependent incompleteness, we use the ETASI model (i.e., ETAS-Incomplete; Hainzl (2016, 2021)) instead of the ETAS model. This new formulation takes into account a rate-dependent incompleteness by adding one parameter T_b , defined as a blind time; for a duration T_b following an earthquake of magnitude M , any event of magnitude less than M cannot be detected. In practice, the ETASI model acts as an apparent rate at every t , considering the likelihood of observing large magnitude events in $[t - T_b, t]$. The ETASI apparent seismicity rate function is (Hainzl, 2021):

$$\lambda(t) \approx \frac{1}{T_b} (1 - e^{-T_b \lambda_0(t)}). \quad (4)$$

From Equation 4, we see that the ETASI rate $\lambda(t)$ is simply the original ETAS rate $\lambda_0(t)$ of Equation 2 modulated by the blind time T_b during high seismicity rate periods. Likewise, the G-R distribution is affected by the rate-dependent incompleteness because some low magnitude earthquakes are undetected. The apparent Gutenberg-Richter distribution at t is (Hainzl, 2021):

$$f(m, t) \approx \beta T_b \lambda_0(t) \frac{e^{-\beta(M-M_c)} e^{T_b \lambda_0(t) e^{-\beta(M-M_c)}}}{1 - e^{-T_b \lambda_0(t)}} \quad (5)$$

From a given catalog ($t_i \in [T_1, T_2]$, $m_i \geq M_c$), we extract the best fitting ETASI parameters by maximizing the following Log-Likelihood function (Hainzl, 2021):

$$\mathcal{L} = \sum_{i=1}^N \ln[f(m_i, t_i)] + \sum_{i=1}^N \ln[\lambda(t_i)] - \int_{T_1}^{T_2} \lambda(t) dt \quad (6)$$

For the ValEq catalog, we extract the best fitting parameters for magnitudes above the magnitude of completeness $M_c = 2$. Moreover, following Davidsen and Baiesi (2016), we impose self-similarity in the aftershock triggering process by fixing $\alpha = \beta$ during the maximization of the likelihood function. With this self-similarity constraint, the probability for a $M = 8$ to trigger $M = 6$ earthquakes is assumed same as the probability for a $M = 4$ to trigger $M = 2$ earthquakes, for example. We tested a case without this self-similarity constraint at the earlier stage of this study, but the resultant branching rate inverted from the ValEq catalog was much larger than 1, leading to a non-stationary synthetic ETAS catalog with an infinite number of aftershocks and increasingly large magnitudes. This constraint also reduces the number of free parameters to 6 as for the classic ETAS model. The best fitting ETASI parameters extracted from the ValEq catalog are presented in Table 1.

To test the reliability of the ETASI Log-Likelihood maximization, we invert the ETASI parameters for 100 synthetic ETASI catalogs (Figure S4 in Supporting Information S1). We use the ETASI parameters extracted from ValEq (Table 1) as the true parameters to generate the synthetic catalogs (Zhuang & Touati, 2015). Results indicate that A , p , $\alpha = \beta$, μ and T_b are well constrained by the parameter estimation and c slightly overestimated but with a reasonably close value. This tendency agrees with the conclusions of Hainzl (2021). They have found a similar bias for c and suggested that it may be explained by the lack of earthquakes during rate-dependent incompleteness. Such incomplete data breaks the triggering links between earthquakes and complicates the estimation of an Omori-Utsu rate decay for individual aftershock sequences. Moreover, after large magnitude earthquakes, the early aftershock rate is mainly controlled by the rate-dependent incompleteness for a period greater than c . It delays the apparent start of the Omori-Utsu rate decay and likely bias the c -value estimation toward higher values. In any case, as suggested by Hainzl (2021), the c -value estimated with the ETASI model is less biased than estimated with the classic ETAS model over incomplete catalogs.

3.2. Testing ValEq Against the ETASI Model

With the best-fitting parameters (Table 1) and Equation 4, we compute the seismicity rate expected from ETASI at any time t in the studied time-period. Integrating this expected seismicity rate over time gives an expected number of earthquakes. We define the cumulative number of earthquakes expected from the best fitting ETASI model, $\tau(t)$, as:

$$\tau(t) = \int_{T_1}^t \lambda(u) du, \quad (7)$$

where, λ is the ETASI rate given by Equation 4 and T_1 is the start time of the catalog. We compare $\tau(t)$ with the observed cumulative number of earthquakes at t , $N_{obs}(t)$. If the best fitting ETASI model explains perfectly the observed seismicity, $\tau(t)$ and $N_{obs}(t)$ must be equal over time. In such a scenario, it implies that we cannot reject the hypothesis that the earthquake sequence can be modeled with a constant background rate and aftershock triggering. Any strong differences between $\tau(t)$ and $N_{obs}(t)$ highlight an anomalous activity with respect to the ETASI model. Representing the predicted seismic activity, $\tau(t)$ as a function of the observed seismic activity, $N_{obs}(t)$ is known as the transformed time analysis introduced by Ogata (1988).

The evolution of $\tau(t)$ and $N_{obs}(t)$ around the mainshock occurrence time is displayed in Figure 2a. In Figure 2b, we display the entire period in the transformed time domain. This transformed time representation enables a simplified comparison of the seismicity over the full duration of the catalog, by gathering periods of low and high seismicity in a single figure. In the transformed time domain, if the seismicity is perfectly explained by the best-fitting ETASI process, $\tau(t)$ and $N_{obs}(t)$ should be equal and thus exhibit a straight line with a slope of 1 (i.e., a unit Poisson rate) with a normal standard deviation of $\sigma(t) = \sqrt{\tau(t) \left(1 - \frac{\tau(t)}{\tau(T_2)}\right)}$ (Ogata, 1992). If the curve significantly diverges from this straight line, we can interpret the local slope as a seismicity deficit (slope < 1) or excess (slope > 1) compared to the ETASI model. They are better illustrated by the difference $N_{obs}(t) - \tau(t)$ (Figure 2), in which the seismicity deficit and excess correspond to negative and positive slopes, respectively. Our results highlight that the seismicity surrounding the Valparaiso mainshock diverges from the ETASI prediction by more than 3σ . We observe three main regimes of seismicity with respect to the best-fitting ETASI model. From the starting time of the catalog and up to the first foreshock, we observe a low negative slope that indicates a small deficit of earthquakes compared to ETASI model. We then observe a significant change toward a positive slope (step $\geq 3\sigma$) highlighting an excess of seismicity, starting within the foreshock sequence and persisting at least 5 days after the mainshock. After that time, the slope slowly returns to its initial low deficit regime. These results indicate that the best fitting ETASI model cannot successfully reproduce the 5-year seismicity variations observed in the area of the 2017 Valparaiso mainshock. Specifically, they suggest that the anomalously high seismic activity observed from -1 day up to at least $+2$ (possibly up to $+5$ days) days after the mainshock is driven by another process that is not captured by our stationary ETAS model. Similar variations of $N_{obs}(t) - \tau(t)$ as reported in Figure 2 are actually observed in synthetic catalogs with a finite duration transient background seismicity over the stationary background rate (see Text S1 and Figure S5 in Supporting Information S1). Such a transient increase of the seismicity in a synthetic catalog produce a similar positive anomaly as in Figure 2 when analyzed with the ETASI model with a constant background rate. Moreover, it also shows that the two periods of low seismic productivity can be explained by the enhanced earthquake activity around the mainshock, because the transient biases the estimation of ETASI parameters toward higher productivity values (i.e., larger values for A in Equation 2).

In order to interpret the observed seismicity excess, we performed additional ETASI inversions that include additional triggering terms during the Valparaiso sequence, modeling a transient triggering. This allows us to quantitatively capture the part of the seismicity that cannot be attributed to background and aftershocks triggering. We first add a transient constant rate, μ_2 , starting at the time of the first foreshock and lasting for an unknown duration T_e days, incremented each $+0.5$ days. We find that, including such a transient background rate can significantly reduce the Akaike Information Criterion (AIC), and thus better explain the seismicity. The AIC allows to compare different models with different parameters by correcting the likelihood (Equation 6) by the number of model parameters k used: $AIC = 2k - 2LLH$ (Akaike, 1974; Ogata, 1989). The best model, with the lowest AIC is obtained when $T_e = 3.5$ days with a rate $\mu_2 = 87.3$ (i.e., ~ 305 events; Figure S6a and Table S1 in Supporting Information S1). However, even with this transient constant rate, a part of the seismicity excess observed after the mainshock is still not well captured. Because the remaining seismicity excess seems causal to the mainshock, we choose to freely invert the magnitude of the mainshock in addition to the transient constant rate. We find (Figure S6.b and Table S1 in Supporting Information S1) that including both the transient and a free mainshock magnitude in the model can further reduce the AIC and can explain all the seismicity excess. The transient constant term is lasting $T_e = 3.5$ days with a rate $\mu_2 = 76.1$ (i.e., ~ 266 events) and the mainshock magnitude is evaluated to $M_{mainshock} = 8.2$. This shows that the seismicity excess can be modeled by a transient rate starting at the time of the foreshock sequence and lasting for 1.5 days following the mainshock time and with an unusually high aftershock productivity for the mainshock. It further supports that the seismicity before and after the mainshock is unusually enhanced with respect to typical magnitude-dependent aftershock triggering and requires external triggering process to be well captured.

3.3. Declustering Approach

To confirm whether the anomalously high seismic activity around the mainshock is a real and significant feature, we employ another declustering approach, which is a modified version of the MISD algorithm of Marsan and Lengline (2008). Our method differs from the original MISD in two aspects: First, as did for the ETAS model, we focus on the temporal variations of the seismicity rate by ignoring the spatial dependence. Second, in addition to the magnitude-dependent aftershock seismicity and the stationary background seismicity, we consider an external forcing process that can trigger an additional seismicity around the mainshock. It models seismicity unrelated to earthquake interaction, such as slow slip driven seismicity. Neglecting any spatial dependence in the original method, the earthquake rate at time t can be expressed as

$$\phi(t) = \phi_0 + \sum_{i, t_i < t} g(m_i, t - t_i) \quad (8)$$

where ϕ_0 is a constant background rate over the whole duration of the catalog T ; m_i and t_i are the magnitude and occurrence time of earthquake i , respectively, and g is a triggering kernel. The method assumes no shape for g but simply considers a piecewise constant discretization in time and magnitude of the kernel such that

$$g_{kt} = g(M_k < m < M_{k+1}, T_l < t < T_{l+1}) \quad (9)$$

where T_p and M_k are the time and magnitude intervals used for discretization, respectively. Based on Equation 8 and an initial guess of g , we can compute the earthquake rate $\phi(t)$ and then the weights ω_{ij} of earthquake i triggering earthquake j and the background weight ω_{0j} . These weights are defined as.

$$\omega_{ij} = \frac{g(m_i, t_j - t_i)}{\phi(t_j)}; \quad \omega_{0j} = \frac{\phi_0}{\phi(t_j)}, \quad (10)$$

$$\sum_{i=1}^{j-1} \omega_{ij} + \omega_{0j} = 1. \quad (11)$$

where the last equation is used for normalization and actually transforms these weights into probabilities. These weights are then used to compute a new estimate of the triggering kernel and the background rate. The process is repeated until reaching the convergence. A detailed description of the algorithm is available in Marsan and Lengliné (2010).

Then, we account for a possible additional seismicity driven by an external process. Similarly to the ETAS analysis, we assume that this external forcing process starts at a time, t_e and lasts for a unknown duration T_e and that this contribution can be modeled with a constant rate, ϕ_e such that the seismicity rate is now described as

$$\phi(t) = \phi_0 + \sum_{i, t_i < t} g(m_i, t - t_i) + \phi_e(\mathcal{H}(t - t_e) - \mathcal{H}(t - t_e - T_e)) \quad (12)$$

where \mathcal{H} is the Heaviside step function. We do not attempt to model the shape of this external triggering process but rather keep a simplified model with a constant rate. Therefore, we introduce the weights $\omega_{ej} = \phi_e/\phi(t_j)$ if $t_e < t_j < t_e + T_e$ and 0 otherwise. The normalization condition becomes $\sum_{i=1}^{j-1} \omega_{ij} + \omega_{0j} + \omega_{ej} = 1$. This additional triggering modifies the likelihood function associated with the original algorithm such that we have now:

$$L = -\phi_0 T - \phi_e T_e + n_0 \phi_0 + n_e \phi_e - \sum_{ij} n_i g_{ij} \delta t_j + \sum_{ij} n_{ij} \ln(g_{ij}), \quad (13)$$

with, n_0 the number of background earthquakes, $n_0 = \sum_i \omega_{0i}$ and $n_e = \sum_i \omega_{ei}$ the number of earthquakes triggered by the external forcing process. The number of earthquakes with magnitude in the interval $[m_i, m_i + 1]$ is noted n_i , while n_{ij} is the number of earthquakes triggered by a magnitude i earthquake in the time interval $[t_j, t_{j+1}]$ of duration δ_j . Based on this approach, we compute the background rate ϕ_0 , the kernel g and the external forcing rate, ϕ_e . As the duration of this external forcing T_e is unknown, we simply estimate it by grid search ranging from 0.01 days up to 30 days. The best parameters are obtained by maximizing L . In order to test the method, we perform a series of synthetic tests to check the ability of the proposed algorithm to recover a transient episode of seismicity (see Text S2 and Figure S7 in Supporting Information S1).

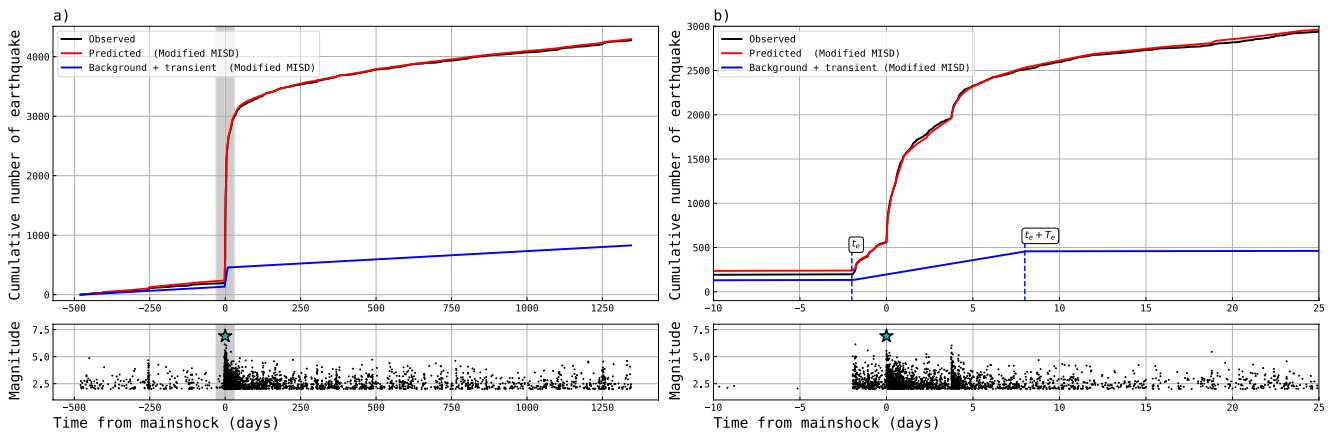


Figure 4. (a) Cumulative count of earthquakes of the ValEq catalog (black) and their prediction by the best fitting modified model-independent stochastic declustering (MISD) (red). (blue) Cumulative count of earthquake declustered by the modified MISD analysis. This include background events and those triggered by the external process ($\sum \omega_{0i} + \omega_{ei}$). Bottom subplot (black dots) shows times and magnitudes of the ValEq catalog. (b) Same as (a) but zoomed in the Gray area. t_e and T_e are respectively the start time and the duration of the external process of our modified MISD model.

We apply the declustering algorithm described above to the ValEq catalog with $t_e = 47$ hr before the occurrence of the Valparaiso mainshock (i.e., the origin time of the first foreshock). We also take into account the time-evolution of the magnitude of completeness following large earthquakes using the approach of Peng et al. (2007) in which a transient magnitude of completeness $m_c(t) = \bar{m}(t) - 1/(b \ln(10))$ is computed with $\bar{m}(t)$ an average magnitude computed over the next N_e earthquakes in time. It follows that an earthquake at time t counts as $n(t) = 10^{m_c(t) - m_e}$. Here, we set $b = 0.74$ as inverted from the ETASI procedure, $m_c = 2$ and we choose $N_e = 10$ as in Marsan and Lengliné (2010). The maximum likelihood, L is obtained with a value of $T_e = 10$ days, corresponding to an inverted value of $\phi_e = 41$ earthquake per day. Such large values of transient duration and rate indicate that a substantial part of the seismicity is not well explained by magnitude-dependent triggering kernels alone. Figure 4 shows the background events and those triggered by the external process (i.e., events that do not result from earthquake interactions). This confirms the previous ETASI analysis that an additional triggering, starting before the Valparaiso mainshock and lasting several days after its occurrence is needed in order to correctly represent the seismicity.

4. Repeater Activity

A slowly creeping subducting interface loads embedded asperities that repeatedly fail over time, producing repeating earthquakes, which are characterized with similar source location and waveforms (Uchida (2019); Kato et al. (2012, 2016)). Such repeater events can then be used to track aseismic slip rates surrounding the ruptured asperities.

To search for repeating events in the vicinity of the 2017 Valparaiso earthquake, we evaluate the similarity of waveforms for all earthquake pairs within the ValEq catalog. We compute an average cross-correlation coefficient (CC) over the seven stations that are associated with the largest number of P and S picks (i.e., MT01, MT09, MT02, VA03, VA06, MT07, and VA05). At every station, the CC is defined as the maximum value of the cross-correlation function between the two waveforms of the earthquake pair. This cross-correlation function is computed in a 40-s time window starting 5 s before the P arrival in the 2–20 Hz band. This large time window allows us to include both P and S arrivals and to maximize the signal-to-noise ratio. The final CC value of the earthquake pair is defined as the average of the CC values computed at available stations. Pairs of events that share less than three stations are automatically discarded. Then, we gather earthquakes with similar waveforms into families based on a hierarchical clustering algorithm using a complete linkage over the CC value. We retain families of earthquakes with a high waveform similarity (i.e., $CC > 0.80$) as a first sub-set of potential repeating earthquakes. Then, we ensure that events within a family are all co-located on the same asperity using the HypoDD double-difference relocation algorithm (Waldhauser & Ellsworth, 2000). For every pair of events, we estimate travel time differences between both P and S phases at all the available stations. Travel time difference between two phases of each event pair is estimated by cross-correlation. For P phase, we use a 5 s window that

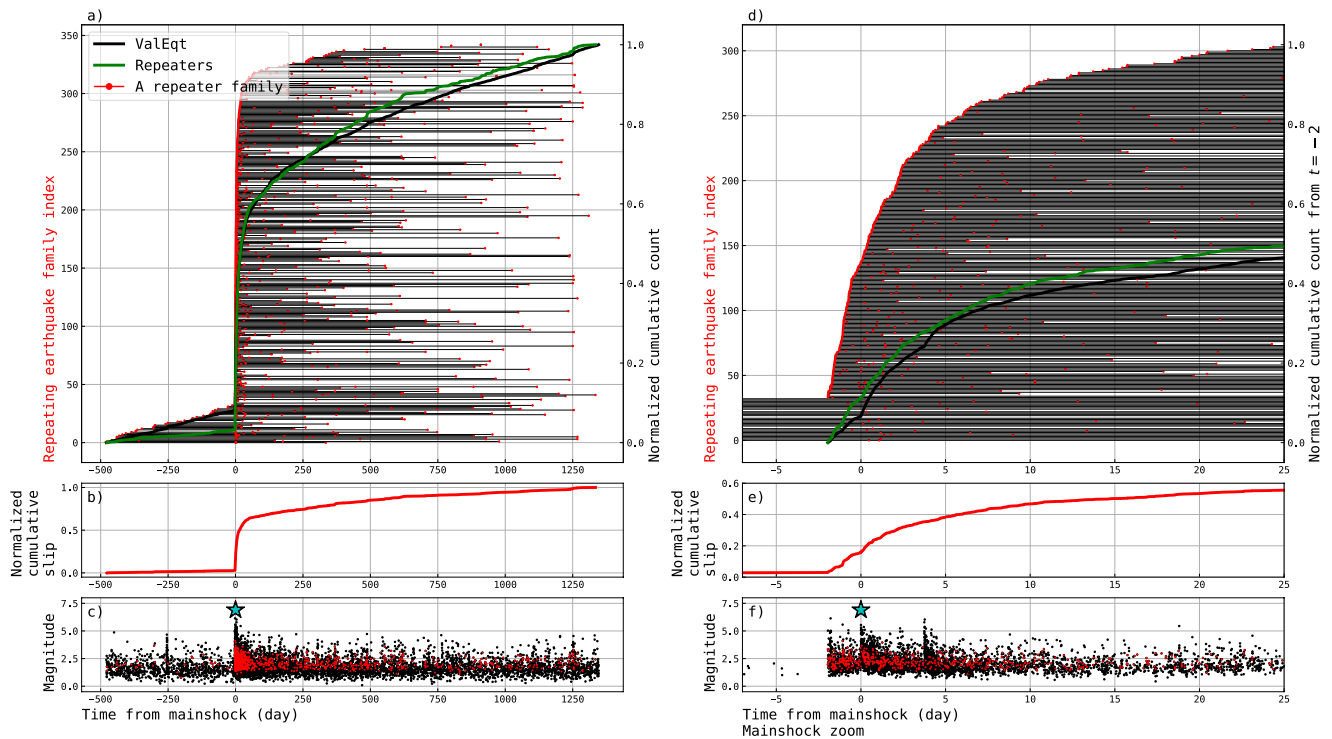


Figure 5. (a) Families of repeating earthquake detected in the ValEqt catalog. A horizontal black line represents one family by connecting the repeating earthquake (red dots). The green and black curves are the normalized cumulative number of repeaters and ValEqt earthquakes respectively. (b) Normalized cumulative slip estimated from repeating earthquakes. (c) Times and magnitudes of ValEqt earthquakes (black dot) and repeating earthquakes (red dot). The blue star indicates the mainshock. Panels (d, e and f) same as (a, b and c) but zoomed in the vicinity of the mainshock time. Note that the normalized cumulative count of repeaters and ValEqt earthquakes starts at $t = -2$ days in panel (d).

starts 1.5 s before the pick. For S phase, we use a 10 s window starting 3 s before the pick. Those traces were previously band-pass filtered with a band width of 2–20 Hz. To evaluate the relocation uncertainties, we relocate events within each family using the SVD solving method of HypoDD, using the CC values as a weight of differential travel-time measurements. On average, a pair of event is relocated with 13 differential travel-time measurements. During the relocation process, we discard events with an inter-event distance greater than 1 km or with an RMS residual greater than 6 times the standard deviation. After the relocation, we estimate a rupture radius for each event by assuming a circular crack model with a stress drop of 3 MPa (Hanks & Bakun, 2002). From relocated hypocenters and their circular rupture radii, we compute the 3D distance between rupture patches for every earthquake pairs within families. Taking hypocenter location uncertainties into account, we further discard events that have less than 80% of chance to intersect with all the other rupture areas of the family. Finally, we discard events within a family with a magnitude difference $\Delta M \geq 1$. With these multiple criteria, high waveform similarity, collocation, and a similar magnitude of all the events in each family can safely be interpreted as actual repeating earthquakes.

Following this approach, we detected 342 repeater families consisting of at least two events (Figures 5 and 6). Across all the families, we identified 1,171 repeating earthquakes. In order to test the robustness of our repeating earthquake analysis, we changed the various thresholds for forming the repeater sequences. It yielded moderate variation in the number of repeaters and number of families, but it does not alter the conclusions presented below, regarding the temporal evolution of the repeater activity. An intense repeater activity initiated during the 2-day foreshock sequence with the highest rate over the whole catalog period. After the mainshock occurrence, the repeater rate decays continuously over the whole analyzed period, but never returns to the initial rate observed before the foreshock sequence. Unlike the seismicity of the ValEqt catalog, the repeaters rate is not strongly impacted by the occurrences of large magnitude earthquakes.

Compared to the earthquakes in the ValEqt catalog, the repeater activity is confined to a small region (Figure 6). The main repeater activity is located in the vicinity of the mainshock hypocenter and a secondary activity is

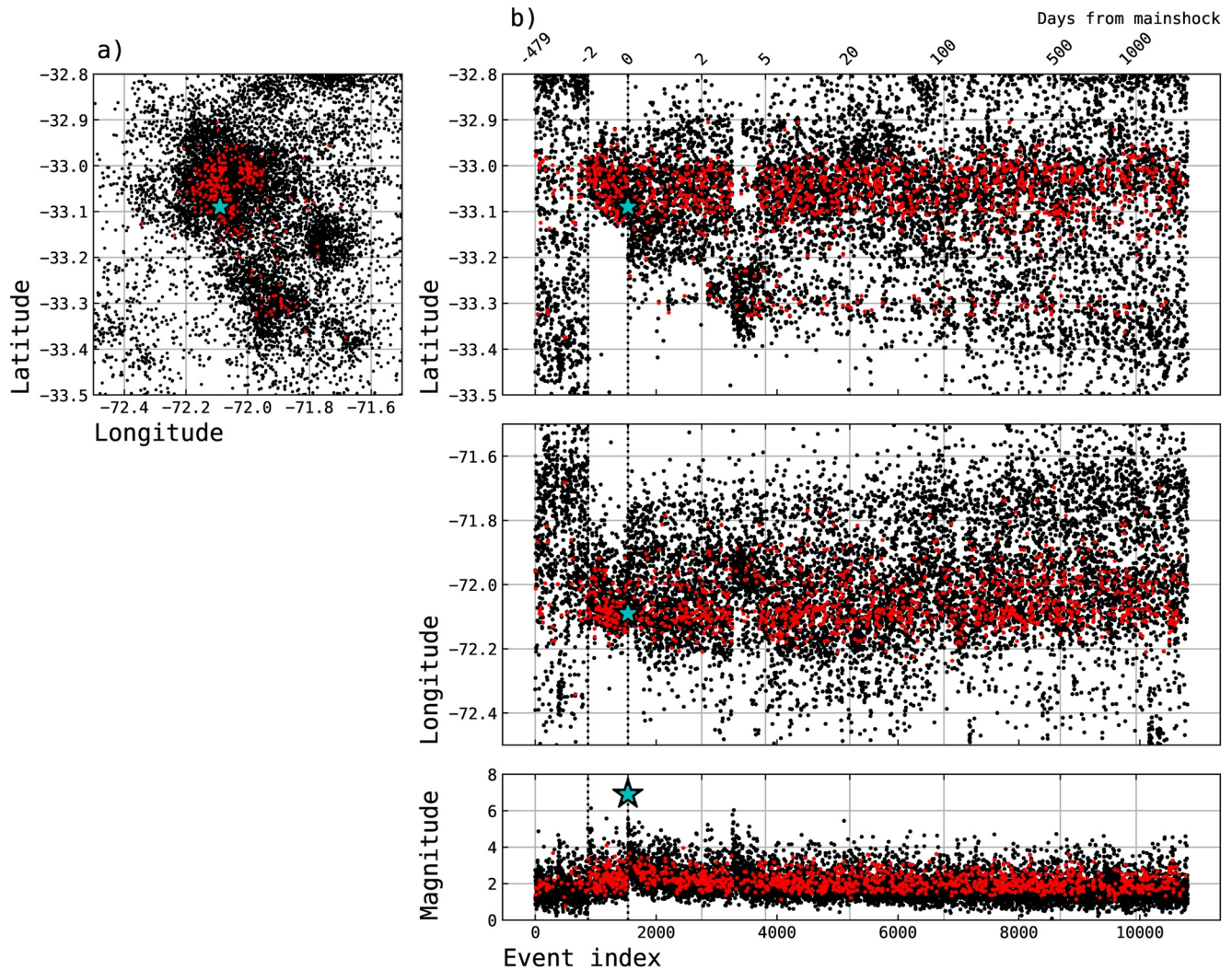


Figure 6. Space and time evolution of the ValEqt seismicity (black dots) and repeating earthquakes (red dots). The light blue star indicates the mainshock. (a) Horizontal distribution of the seismicity. (b) Latitudes, longitudes and magnitudes against the chronological index of the ValEqt seismicity. The chronological index shown by the bottom horizontal axis ticks for each subplot. The corresponding time (days from mainshock) is shown with the top horizontal axis ticks. The two vertical dotted lines highlight the indices/timings of the first foreshock and the mainshock.

observed to the south before and after the largest aftershock. During the foreshock sequence, the repeater activity and the seismicity are almost perfectly co-located. After the mainshock, the repeater activity remains exclusively located at the initial foreshock location, unlike the seismicity that spreads to a wider area.

The aforementioned observations indicate that the repeater activity does not behave as a random subset of the seismicity. Repeaters seem to be driven by a specific process that initiates before the mainshock and extend after it, within a specific area delimited by the foreshock activity. Moreover, the repeater activity appears to decay continuously over time and is not strongly affected by the occurrence of large earthquakes, nor the mainshock. The intense repeater activity observed during the foreshock sequence recalls the occurrence of the pre-mainshock aseismic transient slip detected by Ruiz et al. (2017) and (Caballero et al., 2021). Using these repeaters, we estimate time-evolution of aseismic slip on the subduction interface over the entire earthquake sequence. We follow the approach of Kato et al. (2012, 2016) using a circular crack model with a constant stress drop of 3 MPa to estimate the individual repeater slip amplitudes (Hanks & Bakun, 2002; Uchida, 2019). Then, individual slip amplitudes are summed over time and averaged by the number of repeater families to estimate cumulative slip evolution (Figure 5). To the first order, the obtained slip rate is maximum at the beginning of the foreshock sequence and slowly decays with time over days to months until the end of the studied time-period. Impacts of large earthquakes

to this steady decay appears very limited (Figure 5). Overall, these results suggest that the transient aseismic slip initiated during the foreshock sequence persists after the mainshock, following a steady rate decay.

5. Aseismic Slip Before and After the Mainshock by High-Rate GPS

The inferred unusual seismic activity (Figures 2 and 4) suggests the presence of a specific triggering process before and after the mainshock. The repeater-based slip rate (Figures 5 and 6) suggests that this triggering process is a transient aseismic slip. Indeed, a transient aseismic slip is reported for the pre-mainshock stage (Caballero et al., 2021; Ruiz et al., 2017), but temporal relationship between the aseismic preslip and the foreshock sequence has remained unclear, which is key to understanding mechanical processes. For the post-mainshock stage, no studies have yet investigated very early postseismic deformation and rapid afterslip associated with the 2017 Valparaiso mainshock. Therefore, to fill the gap between the two stages, we use high-rate GPS (hereafter, HRGPS) to investigate transient slip during the whole 2017 sequence as independent observable from the seismicity analysis. We directly interpret pre- and post-seismic HRGPS time series as proxy of slow slip in this study; Viscoelastic relaxation is the other dominant mechanism responsible for postseismic deformation in subduction zones, but their contribution would be negligible given the mainshock magnitude and time scale considered in this study (e.g., Periollat et al., 2022; Sun & Wang, 2015; Wang et al., 2012).

We employ 5-min coordinates between 30 days before and after the day of the mainshock at 6 sites near the epicenter (Figure S8 in Supporting Information S1) (Caballero et al., 2021), processed by Nevada Geodetic Laboratory (Blewitt et al., 2018). Nominal errors of these coordinates are ~ 7 and ~ 9 mm for east and north components, respectively. These coordinates are estimated by a Kalman filter and smoother with 17 m of the scale of random-walk process (Blewitt et al., 2018), so forward and backward propagations of the sudden coseismic offsets unlikely happened. We do not use sites VALN and CUVI (Figure S8 in Supporting Information S1) because 5-min coordinates of the former are too noisy and those of the latter are not available. The original coordinates are affected by a high noise level, so we post-process the series to alleviate the fluctuations (Figure S9 in Supporting Information S1). We first fix the coordinates into the South American plate reference frame by using its Euler pole with respect to ITRF2014 (Altamimi et al., 2017) (black dots in Figure S9 in Supporting Information S1). Then, we remove the fluctuations associated with multipath (i.e., Choi et al., 2004; Itoh & Aoki, 2022; Larson et al., 2007; Ragheb et al., 2007), which is estimated as a seasonal component of “Seasonal-Trend decomposition using LOESS (STL)” (Cleveland et al., 1990; Pedregosa et al., 2011) with a period of 86,100 s. This period is the closest integer multiple of the sampling interval to a typical repeat period of multipath signature (86,154 s; Ragheb et al., 2007). Then, the multipath free time series (red in Figure S9 in Supporting Information S1) is corrected for a diurnal variation component following the same procedure as the multipath removal but with a repeat period of 86,400 s in order to obtain diurnal fluctuations free series (purple in Figure S9 in Supporting Information S1).

Next, we remove common mode fluctuation at all the sites, which are primarily due to fluctuation of reference frame and uncertainty of satellite orbits (e.g., Wdowinski et al., 1997). We extract common mode fluctuation (orange in Figure S9 in Supporting Information S1) by stacking coordinate time series at distant sites from the source area (Figure S8 in Supporting Information S1). Before stacking, we remove some outliers and the linear trend. Here, outliers are defined as epochs satisfying Equation 14 (Itoh et al., 2022).

$$\left| x_i - \frac{q_1 + q_3}{2} \right| > n * \frac{q_3 - q_1}{2} \quad (14)$$

where, x_i is displacement at the i -th epoch, q_1 and q_3 are the 25 and 75 percentile values of the position time series, respectively, and n is a threshold which was set to eight in this study. The linear trend is estimated from the time series without outliers. The extracted common mode fluctuation is subsequently subtracted from the time series at the six sites of interest (blue in Figure S9 in Supporting Information S1).

Then, we remove the pre-mainshock trend from the common mode free time series. The linear trend is estimated from the data between 30 and 10 days before the mainshock. The trend is extrapolated to the subsequent period. Finally, we stack the cleaned time series at BN05 and TRPD, which are only ~ 5 km apart, to further reduce the noise level (Figures S10 and S11 in Supporting Information S1). For stacking, the two time series are weighted according to the inverse of the square of quartile deviation of time series from 30 to 10 days before the mainshock. Hereafter, we assign a pseudo-name of site STAC to the stacked time series for the ease of writing and discussion.

Finally, we remove mainshock coseismic offsets from the time series at all sites (Figure 7, Figures S12 and S13 in Supporting Information S1). We also remove the offset caused by the largest aftershock that is visible on the time series at QTAY (Figure 7). We calculate the mainshock offsets as a difference between pre- and post-event positions, which were defined as average positions during 1 and 0.5 days before and after the event, respectively. The same procedure is applied to the largest aftershock except for the post-event window length set to be 1 day. Interestingly, at the coastal sites (QTAY and STAC consisting of BN05 and TRPD), the steep trend following the mainshock coseismic step (red in Figure 7) was not significantly discernible after the step removal. Investigating their origin is beyond the scope of this study, but we speculate that they are just occasional deviation of GPS time series which are divided by the mainshock step happening somewhat during this deviation.

The stacked time series at STAC, closest to the mainshock epicenter, clearly exhibits a westward motion before, during, and after the mainshock (Figure 7). The pre-mainshock transient motion started ~ 3 days before the mainshock and ~ 1 day before the first foreshock. No acceleration of displacements is discernible before the mainshock, which can be interpreted as no acceleration of aseismic slip toward the mainshock. Coseismic displacement associated with the largest foreshock is not resolved and possibly buried in the remaining noise given the expected amplitude (Caballero et al., 2021). Interestingly, the transient trenchward motion continues smoothly before and after the mainshock and lasted ~ 20 days (green in Figure 7). In other words, there is no notable acceleration of motion following the mainshock. Such an apparent lack of mainshock-induced acceleration is also seen in the daily GPS coordinates across the mainshock time (Ruiz et al., 2017). Furthermore, the site motion did not change its direction across the mainshock occurrence time (Figure S14 in Supporting Information S1) and the coseismic displacement also points in the same direction. Similarly, continuous transient westward motion before and after the mainshock is visible with smaller amplitudes at QTAY, ~ 20 km south of STAC (Figure 7). At the other three sites away from the source area, namely, CTPC, RCSD, and ROB1, the transient motion before the first foreshock is less convincing but the moving median curve demonstrate slight deviation from the trend. The non-uniform but coherent trenchward pattern of postseismic motion several days before and after the mainshock excludes the possibility that they represent local artifacts (Figures S10 and S14 in Supporting Information S1). The north component of GPS coordinate time series does not exhibit discernible pre-mainshock motion but post-mainshock motion is visible at CTPC, RCSD, and ROB1 (Figure S11 in Supporting Information S1). Based on these predominantly trenchward motions at the multiple sites in the same direction across the mainshock occurrence time (Figure S14 in Supporting Information S1) and without abrupt changes in their direction and rate, we conclude that the HRGPS observations indicate the occurrence of a continuous aseismic slip transient along the megathrust.

6. Discussion and Conclusions

In this study, we have investigated the seismic and aseismic processes during the 2017 Valparaiso earthquake sequence, from the time of the first foreshocks to the end of the post-seismic sequence. We have built a high resolution catalog of the seismicity from 2016 to 2021, improving the completeness by 1 magnitude unit compared to the local CSN catalog. Thanks to this catalog, we have tested whether the seismicity can be explained by a stationary background term, that may describe a constant tectonic loading, and aftershock triggering. We showed that the stationary hypothesis cannot accurately describe the observed seismicity, particularly before and after the mainshock. Two different temporal magnitude-dependent aftershock triggering models (i.e., ETASI and MISD models) have shown that the seismicity from the foreshock sequence up to several days after the mainshock (2 and 8 days, respectively) is more abundant than predicted. This result suggests the presence of an additional forcing superimposed to the stationary background and magnitude-dependent aftershock triggering. Such a transient forcing term may be linked to an increase of the slip rate on the interface which has been already suggested for the pre-seismic period of the Valparaiso sequence (Caballero et al., 2021; Ruiz et al., 2017). To better document a potential increase in slip rate on the interface and its temporal variation, we have used repeating earthquake and HRGPS positions during the entire sequence, including during the days following the mainshock. Assuming that the repeater rate is directly linked to the slip rate, our results indicate that a transient perturbation of the slip rate begins with the start of the foreshock sequence and decays over days to months without a clear termination. At the first order, the steady decay of the estimated slip rate during the Valparaiso sequence indicates that the mainshock and other large earthquakes have a limited impact on its temporal evolution. Using HRGPS data, we have confirmed the previously reported slow slip during the foreshock sequence and found that it started ~ 1 day before the first foreshock occurrence. The HRGPS data also indicate a quite steady decelerating westward motion

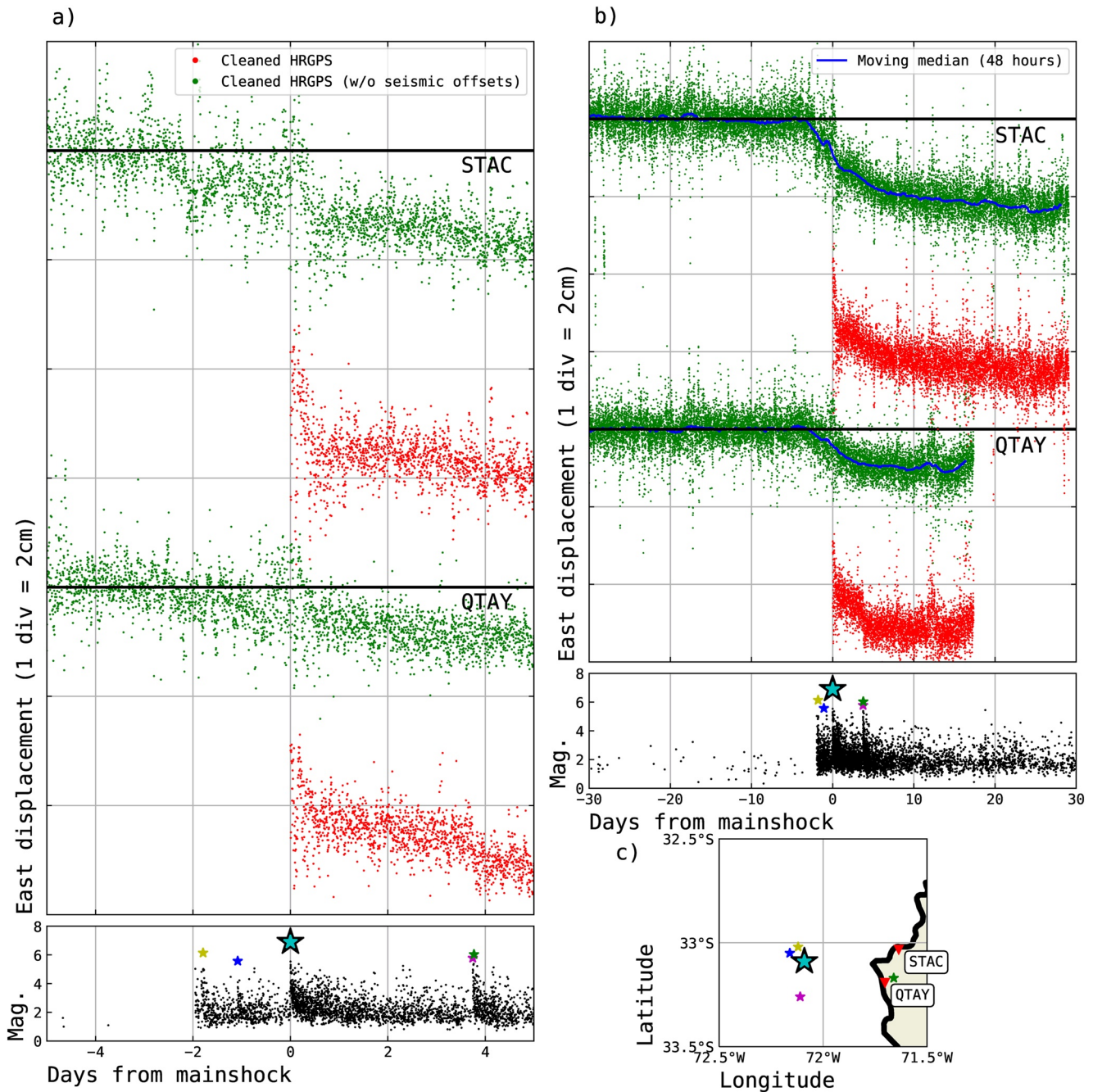


Figure 7. Comparison of high-rate GPS displacements and seismicity evolution before and after the 2017 Valparaiso mainshock. (a) Red and green dots indicate cleaned east positions between 5 days before and after the mainshock with and without seismic offsets, respectively, at the two closest sites QTAY and STAC (location shown in panel (c)). Note that STAC is a pseudo-site name assigned to stacked time series of TRPD and BN05 (See text and Figure S8 in Supporting Information S1 for details). Black dots at the bottom panel indicate magnitude of detected seismicity. Notable large earthquakes are marked with stars, epicenters of which are shown in panel (c). (b) Same as (a) but with data between 30 days before and after the mainshock. A moving median with a window length of 48 hr, calculated from the data without coseismic offsets, is shown in blue for each site. (c) Site location (red inverted triangles) and epicenters (stars with corresponding colors with panels (a) and (b)). The same figure but for all available HRGPS sites is shown in Figure S10 in Supporting Information S1 for east displacement and S11 for north displacement.

since its emergence before the first foreshock up to 20 days after mainshock (Figure 7). This steady westward displacement, preceding the mainshock and persisting after it, is broadly consistent with the slip rate inferred from repeaters. This finding supports the idea that the post-mainshock aseismic slip may be the continuation of the pre-mainshock aseismic slip transient. Finally, both the seismicity and the HRGPS observations show no evidence of slip acceleration prior to the mainshock.

In order to compare our different observations, we summarize the results of our three analyses in Figure 8. We observe that the analyzed signals do not perfectly agree with each other and indicate different start and end times of the identified transient. Setting the mainshock time as $t = 0$, the seismicity excess is evidenced from -1.5 to at least 2 days for the ETASI analysis and from -2 to 8 days for the MISD analysis. The repeating earthquakes track a transient aseismic slip since the occurrence time of first foreshock (-2 days) up to months after the mainshock while the HRGPS suggests that the transient aseismic slip initiates at about -3 days (i.e., ~ 1 day before the first foreshock) and persists at least for 20 days after the mainshock. Such differences originate from different sensitivity of geodetic and seismic observations to interface slip. Our land-based geodetic measurements reflect slip along a large area of the subduction interface. On the other hand, the statistical seismicity analysis is representative of the process taking place only at the location of each earthquake. Repeating earthquakes provide localized, but sparse in situ measurements of the slip rate on a limited area of the interface (Figure 6). Defining the exact interplay between all of these observations is challenging. Still, all these signals consistently demonstrate the same sliding behavior on the interface, with an enhanced slip rate extending over several days both before and after the mainshock.

The difference of slip behavior inferred from our various observations may also partly result from uncertainties and hypotheses inherent to each analysis. As earthquakes interact in space, the ETAS and MISD models are often used with a spatial kernel to weight inter-event distances in the aftershock triggering scheme (Zhuang et al., 2011). However, in this study, we focus only on the temporal variations of seismicity, as spatial considerations would likely complicate the aftershock triggering association in a small study area like ours. Because of earthquake location uncertainties due to the geometry of our network, the inter-event distance is not well constrained and may lead to unrealistic event association. Yet, thanks to our spatial selection, the ValEq seismicity is sufficiently isolated and clustered around the mainshock to be analyzed temporally (see Section 2; Figure 1). We also acknowledge that the repeating earthquake detection and the inferred slip rate is prone to multiple uncertainties. First, the repeating earthquake detection is also impacted by the rate dependent incompleteness mentioned in Section 3. As we cannot detect a lot of low magnitude earthquakes when the seismicity rate is high, we also miss possible repeaters. Such incompleteness may impact the slip rate inferred just after the mainshock and other large earthquakes. Moreover, when the seismicity rate is high, the 40 s cross-correlation window is likely to screen several successive waveforms and further blur the detection of potential repeaters. To evaluate the influence of the window length, we also performed the repeater detection using a smaller cross-correlation windows centered only on the P phases. We obtained more repeater families for the same CC threshold, but with similar conclusions as the ones presented here (see Figure S15 in Supporting Information S1). Second, the repeater rupture sizes and slips are estimated with the standard scaling laws and a priori values (i.e., stress-drop, shear modulus). Using a different scaling law or stress drop (Hanks & Bakun, 2002; Nadeau & Johnson, 1998; Uchida, 2019) yield slightly different repeater families and absolute slip estimates, but still we can draw similar conclusions (see Table S2 and Figure S16 in Supporting Information S1). In order to minimize the influence of these choices, we focus our analysis of slip only on its temporal evolution pattern and not on its absolute amount. Finally, to support our current selection criteria for the co-location of our repeaters (i.e., 80% chance of intersecting rupture front, taking into account relocation uncertainties), we also performed a more selective screening process based on the percentage of rupture overlap between repeaters. Because the relocation uncertainties from HypoDD are found to be significantly smaller than the average circular fracture radii of our repeaters (see Figure S17 in Supporting Information S1), we neglect here relocation uncertainties. From the relocated hypocenters and their circular rupture area, we calculate the percentage of overlap between rupture patches for each earthquake pair within families and discard events that have less than 80% overlap with all other rupture areas in the family. The resulting repeater selection and aseismic slip estimate are almost unchanged and lead to similar conclusions (see Figure S18 in Supporting Information S1), which support our initial selection criterion. The HRGPS data contains noise inherent to the processing strategy, which were not completely removed in this study. The remaining noise limits the possibility to capture second order features of the slab interface processes, such as an accelerated slip just before the mainshock. Moreover, our HRGPS displacements can contain seismic slip contributions (e.g., Caballero et al., 2021). However, Caballero et al. (2021) found that the contribution of $M < 6$ earthquakes to GNSS displacements is very limited, even when accounting for the cumulative moment induced by micro-earthquakes. Therefore, after removing the co-seismic offset of the mainshock and the offsets induced by other large earthquakes, it is reasonable to assume that our HRGPS displacements predominantly represent the contribution of aseismic slip.

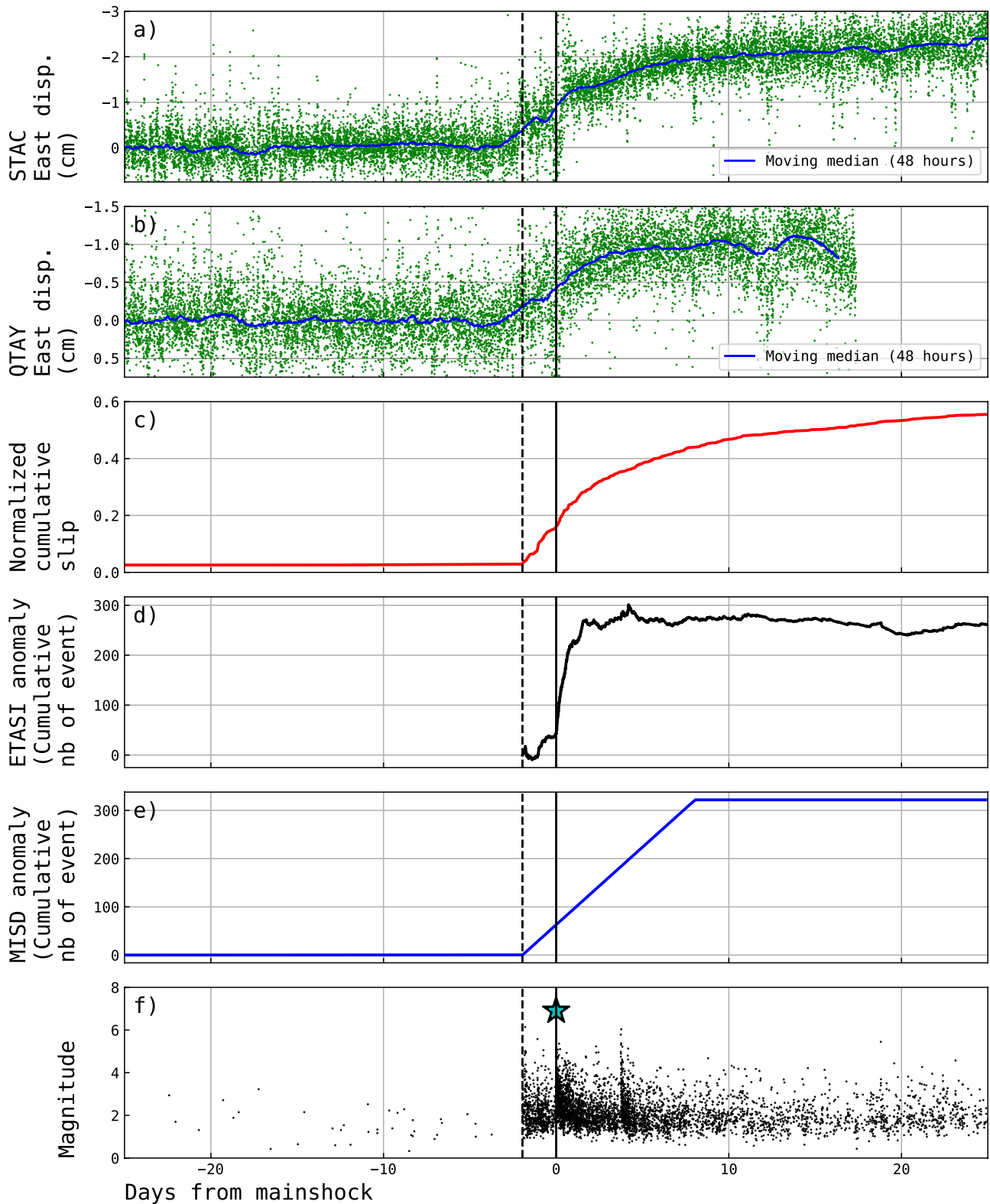


Figure 8. Summary of the seismic and geodetic measurements presented in this study. Panels (a) and (b) cleaned HRGPS east positions at sites QTAY and STAC with the co-seismic steps removed (see Figure 7). (c) Normalized cumulative slip estimated from repeating earthquake (see Figure 5). (d) Cumulative number of event unexplained by the ETASI model since the time of the first foreshock (see Figure 2). (e) Cumulative number of event triggered by the external forcing in the model-independent stochastic declustering analysis (see Figure 4). (f) Times and magnitudes of ValEqt earthquakes. The blue star indicates the mainshock.

In spite of the aforementioned limitations, our observations bring new insights on the possible mechanisms that have driven the 2017 Valparaiso seismic sequence. We show that both the transient aseismic slip and the seismicity excess are not restricted to the foreshock sequence but persist after the mainshock for several days. Repeating earthquakes along with HRGPS time series indicate a continuous aseismic slip transient before and after the mainshock with no significant jump in the slip rate and direction at the time of the mainshock (Figures 8a and b), although an acceleration related to afterslip would have been expected after earthquakes with $M \sim 7$ or greater (e.g., Itoh et al., 2019; Marone et al., 1991; Miura et al., 2006; Periolat et al., 2022). Although Figure 8c depicts slip and displacement variations associated with large earthquakes in the Valparaiso sequence, these temporal changes are small compared with the long-term transient starting before and persisting after the mainshock. This relative continuity of the aseismic transient raises the question of whether the pre- and post-mainshock processes should be interpreted as a single process or as two distinct fault processes that are separated by the mainshock. The commencement of an afterslip with a similar slip rate as the slow slip rate observed immediately before the mainshock seems quite unlikely. In addition, if the post-mainshock aseismic slip is only an afterslip triggered by the mainshock and distinct from the pre-mainshock aseismic slip, we may expect it to approximately scale with the mainshock magnitude (Alwahedi & Hawthorne, 2019; Churchill et al., 2022) and with the aftershocks activity (Hsu et al., 2006; Perfettini & Avouac, 2007; Perfettini et al., 2018). Therefore, it does not explain why we still observe a seismicity excess after the Valparaiso mainshock, that is quite over-productive given the mainshock magnitude (see Section 3). Our observations may rather suggest a unique transient aseismic process persisting during the whole sequence, with very little slip-rate fluctuation induced by large earthquakes. This interpretation of persisting slow slip event is consistent with observations of a continuously enhanced foreshock and post-mainshock seismicity previously reported by Marsan et al. (2014). They showed that worldwide mainshocks preceded by an enhanced foreshock seismicity are also associated with an over-productive aftershock activity and likely requiring an external triggering process such as aseismic slip transient or/and fluid migrations that occur before and after the mainshock occurrence.

Observed precursory aseismic slip is sometimes interpreted as a nucleation phase of the mainshock slowly accelerating toward dynamic rupture by referring to experimental and numerical simulation studies (Ampuero & Rubin, 2008; Das & Scholz, 1981; Dieterich, 1992; Latour et al., 2013; Ohnaka, 1992). In this model, monitoring foreshocks (small asperities loaded by the slipping interface) and the aseismic slip may help to track the ongoing rupture and carry a strong predictive power on the subsequent mainshock occurrence. In the case of the 2017 Valparaiso earthquake, however, there is no clear evidence that pre-mainshock seismic and aseismic processes culminate with the mainshock but rather seems to persist after it. Therefore, they probably cannot be interpreted as a tracer of an accelerating pre-slip nucleation phase. Our results rather indicate that the transient aseismic slip is not directly linked to the occurrence of the mainshock rupture, but acts as an aseismic loading of locked asperities on the fault, and potentially triggering them (Meng & Duan, 2022). Large earthquakes triggered by aseismic loading processes have already been observed in several regions that are frequently associated with slow slip events. Radiguet et al. (2016) showed that recurrent slow slip events with no subsequent large earthquakes was observed on the same interface for years, just next to a large locked asperities, but it finally triggered the 2014 $M_w = 7.3$ Papanoa earthquake. Interestingly, the results of Radiguet et al. (2016) show a slight acceleration of displacements following the Papanoa mainshock, which remain small compared to the overall amplitude of the slow slip event. Similar recurrent slow-slip observations were associated with the triggering of the 2012 $M_w = 7.6$ earthquake in Costa Rica (Voss et al., 2018) or the 2020 $M_w = 6.9$ mainshock in the Atacama region in Chile (Klein et al., 2023), that was also followed with unusually large post-seismic displacements. There are also numerous examples of slow slip events that have been associated with seismicity swarms but not followed by a large mainshock (Lohman & McGuire, 2007; Nishikawa et al., 2021; Vallée et al., 2013). The complex interactions between slow slip and large earthquakes, as evidenced by all these observations, indicate that a transient aseismic slip alone cannot reliably serve as an indicator of an impending mainshock. For the Valparaiso 2017 sequence, the aseismic slip transient initiated just before the first foreshock, may have loaded asperities of the fault plane, triggering seismicity until several days after the mainshock. It suggests that the Valparaiso mainshock behaves as any other seismic asperities, with a probability of occurrence simply mediated by the transient aseismic slip loading. Therefore, to properly address the precursory nature of unusual aseismic and seismic activities, our results suggest that earthquake sequences need to be continuously analyzed, including both foreshock to post-mainshock observations. Although this model may not appear as deterministic as the nucleation phase model, the real-time monitoring of transient aseismic slip and enhanced seismicity can still provide useful additional information about the state of seismic hazard on aseismically slipping faults.

Data Availability Statement

Broadband seismological data are provided by the National Seismological Center (CSN) of the University of Chile through the Incorporated Research Institutions for Seismology Data Management Center (IRIS-DMC) under networks C1.

The High rate GPS positions provided by Nevada Geodetic Laboratory, University of Nevada, Reno are available at <http://geodesy.unr.edu/>.

Our catalog of earthquakes and repeating earthquakes (Moutote et al., 2023) can be found at: <https://zenodo.org/record/8077490>.

Phase picking software EQTransformer (Mousavi et al., 2020b) can be found at: <https://github.com/smousavi05/EQTransformer>.

Phase association software REAL (Zhang et al., 2019b) can be found at: <https://github.com/Dal-mzhang/REAL>.

The location software NonLinLoc (Lomax, 2017) can be found at: <http://alomax.free.fr/nlloc/>

The double difference relocation software HypoDD (Waldhauser & Ellsworth, 2010) can be found at: <https://www.ldeo.columbia.edu/~felixw/hypoDD.html>.

References

- Akaike, H. (1974). A new look at the statistical model identification. *IEEE Transactions on Automatic Control*, 19(6), 716–723. <https://doi.org/10.1109/TAC.1974.1100705>
- Altamimi, Z., Métivier, L., Rebeschung, P., Rouby, H., & Collilieux, X. (2017). ITRF2014 plate motion model. *Geophysical Journal International*, 209(3), 1906–1912. <https://doi.org/10.1093/gji/ggx136>
- Alwahedi, M. A., & Hawthorne, J. C. (2019). Intermediate-magnitude postseismic slip follows intermediate-magnitude (m 4 to 5) earthquakes in California. *Geophysical Research Letters*, 46(7), 3676–3687. <https://doi.org/10.1029/2018GL081001>
- Ampuero, J.-P., & Rubin, A. M. (2008). Earthquake nucleation on rate and state faults—Aging and slip laws. *Journal of Geophysical Research*, 113(B1), B01302. <https://doi.org/10.1029/2007JB005082>
- Barrientos, S., & National Seismological Center (CSN) Team. (2018). The seismic network of Chile. *Seismological Research Letters*, 89(2A), 467–474. <https://doi.org/10.1785/0220160195>
- Blewitt, G., Hammond, W. C., & Kreemer, C. (2018). Harnessing the GPS data explosion for interdisciplinary science. *Eos*, 99. <https://doi.org/10.1029/2018EO104623>
- Bouchon, M., Durand, V., Marsan, D., Karabulut, H., & Schmittbuhl, J. (2013). The long precursory phase of most large interplate earthquakes. *Nature Geoscience*, 6(4), 299–302. <https://doi.org/10.1038/ngeo1770>
- Bouchon, M., Karabulut, H., Aktar, M., Özalaybey, S., Schmittbuhl, J., & Bouin, M.-P. (2011). Extended nucleation of the 1999 mw 7.6 Izmit Earthquake. *Science*, 331(6019), 877–880. <https://doi.org/10.1126/science.1197341>
- Brodsky, E. E., & Lay, T. (2014). Recognizing foreshocks from the 1 April 2014 Chile earthquake. *Science*, 344(6185), 700–702. <https://doi.org/10.1126/science.1255202>
- Caballero, E., Chounet, A., Duputel, Z., Jara, J., Twardzik, C., & Jolivet, R. (2021). Seismic and aseismic fault slip during the initiation phase of the 2017 $M_w = 6.9$ Valparaíso earthquake. *Geophysical Research Letters*, 48(6), e2020GL091916. <https://doi.org/10.1029/2020GL091916>
- Choi, K., Bilich, A., Larson, K. M., & Axelrad, P. (2004). Modified sidereal filtering: Implications for high-rate GPS positioning. *Geophysical Research Letters*, 31(22), L22608. <https://doi.org/10.1029/2004GL021621>
- Churchill, R. M., Werner, M. J., Biggs, J., & Fagereng, A. (2022). Afterslip moment scaling and variability from a global compilation of estimates. *Journal of Geophysical Research: Solid Earth*, 127(4), e2021JB023897. <https://doi.org/10.1029/2021JB023897>
- Cleveland, R. B., Cleveland, W. S., McRae, J. E., & Terpenning, I. (1990). StI: A seasonal-trend decomposition. *Journal of Official Statistics*, 6(1), 3–73.
- Das, S., & Scholz, C. H. (1981). Theory of time-dependent rupture in the Earth. *Journal of Geophysical Research*, 86(B7), 6039–6051. <https://doi.org/10.1029/JB086iB07p06039>
- Davidson, J., & Baiesi, M. (2016). Self-similar aftershock rates. *Physical Review E*, 94(2), 022314. <https://doi.org/10.1103/PhysRevE.94.022314>
- de Arcangelis, L., Godano, C., & Lippiello, E. (2018). The overlap of aftershock coda waves and Short-Term postseismic forecasting. *Journal of Geophysical Research: Solid Earth*, 123(7), 5661–5674. <https://doi.org/10.1029/2018JB015518>
- Dieterich, J. H. (1992). Earthquake nucleation on faults with rate- and state-dependent strength. *Tectonophysics*, 211(1), 115–134. [https://doi.org/10.1016/0040-1951\(92\)90055-B](https://doi.org/10.1016/0040-1951(92)90055-B)
- Dodge, D. A., Beroza, G. C., & Ellsworth, W. L. (1995). Foreshock sequence of the 1992 Landers, California, earthquake and its implications for earthquake nucleation. *Journal of Geophysical Research*, 100(B6), 9865–9880. <https://doi.org/10.1029/95JB00871>
- Dodge, D. A., Beroza, G. C., & Ellsworth, W. L. (1996). Detailed observations of California foreshock sequences: Implications for the earthquake initiation process. *Journal of Geophysical Research*, 101(B10), 22371–22392. <https://doi.org/10.1029/96JB02269>
- Durand, V., Bentz, S., Kwiatek, G., Dresen, G., Wollin, C., Heidbach, O., et al. (2020). A two-scale preparation phase preceded an mw 5.8 earthquake in the sea of Marmara offshore Istanbul, Turkey. *Seismological Research Letters*, 91(6), 3139–3147. <https://doi.org/10.1785/0220200110>
- Ellsworth, W. L., & Bulut, F. (2018). Nucleation of the 1999 Izmit earthquake by a triggered cascade of foreshocks. *Nature Geoscience*, 11(7), 531–535. <https://doi.org/10.1038/s41561-018-0145-1>
- Felzer, K. R., Abercrombie, R. E., & Ekström, G. (2004). A common origin for aftershocks, foreshocks, and multiplets. *Bulletin of the Seismological Society of America*, 94(1), 88–98. <https://doi.org/10.1785/0120030069>
- Gomberg, J. (2018). Unsettled earthquake nucleation. *Nature Geoscience*, 11(7), 463–464. <https://doi.org/10.1038/s41561-018-0149-x>
- Hainzl, S. (2016). Apparent triggering function of aftershocks resulting from rate-dependent incompleteness of earthquake catalogs. *Journal of Geophysical Research: Solid Earth*, 121(9), 6499–6509. <https://doi.org/10.1002/2016JB013319>
- Hainzl, S. (2021). ETAS-approach accounting for short-term incompleteness of earthquake catalogs. *Bulletin of the Seismological Society of America*. <https://doi.org/10.1785/0120210146>

Acknowledgments

Discussion with Mathilde Radiguet for HRGPS post-processing was fruitful. This work was supported by the European Research Council (ERC) (under the European Union's Horizon 2020 research and innovation program under Grants 805256 and 865963). Y.I. is an Overseas Research Fellow of the Japan Society of the Promotion of Science. We thank editors Satoshi Ide, an anonymous associate editor, Marino Protti, and two anonymous reviewers for their comments which helped improve the manuscript.

- Hanks, T. C., & Bakun, W. H. (2002). A bilinear source-scaling model for M-log A observations of continental earthquakes. *Bulletin of the Seismological Society of America*, 92(5), 1841–1846. <https://doi.org/10.1785/0120010148>
- Helmstetter, A., & Sornette, D. (2003). Foreshocks explained by cascades of triggered seismicity. *Journal of Geophysical Research*, 108(B10), 2457. <https://doi.org/10.1029/2003JB002409>
- Hsu, Y.-J., Simons, M., Avouac, J.-P., Galetzka, J., Sieh, K., Chlieh, M., et al. (2006). Frictional afterslip following the 2005 Nias-Simeulue earthquake, Sumatra. *Science*, 312(5782), 1921–1926. <https://doi.org/10.1126/science.1126960>
- Igarashi, T., Matsuzawa, T., & Hasegawa, A. (2003). Repeating earthquakes and interplate aseismic slip in the Northeastern Japan subduction zone. *Journal of Geophysical Research*, 108(B5), 2249. <https://doi.org/10.1029/2002JB001920>
- Itoh, Y., & Aoki, Y. (2022). On the performance of position-domain sidereal filter for 30-s kinematic GPS to mitigate multipath errors. *Earth Planets and Space*, 74(1), 1–20. <https://doi.org/10.1186/s40623-022-01584-8>
- Itoh, Y., Aoki, Y., & Fukuda, J. (2022). Imaging evolution of Cascadia slow-slip event using high-rate GPS. *Scientific Reports*, 12(1), 1–12. <https://doi.org/10.1038/s41598-022-10957-8>
- Itoh, Y., Nishimura, T., Ariyoshi, K., & Matsumoto, H. (2019). Interplate slip following the 2003 Tokachi-Oki earthquake from ocean bottom pressure gauge and land GNSS data. *Journal of Geophysical Research: Solid Earth*, 124(4), 4205–4230. <https://doi.org/10.1029/2018jb016328>
- Kagan, Y. Y. (2004). Short-Term properties of earthquake catalogs and models of earthquake source. *Bulletin of the Seismological Society of America*, 94(4), 1207–1228. <https://doi.org/10.1785/012003098>
- Kaneko, Y., & Ampuero, J.-P. (2011). A mechanism for preseismic steady rupture fronts observed in laboratory experiments. *Geophysical Research Letters*, 38(21), L21307. <https://doi.org/10.1029/2011GL049953>
- Kato, A., Fukuda, J., Kumazawa, T., & Nakagawa, S. (2016). Accelerated nucleation of the 2014 Iquique, Chile Mw 8.2 earthquake. *Scientific Reports*, 6(1), 24792. <https://doi.org/10.1038/srep24792>
- Kato, A., Obara, K., Igarashi, T., Tsuruoka, H., Nakagawa, S., & Hirata, N. (2012). Propagation of slow slip leading up to the 2011 Mw 9.0 Tohoku-Oki earthquake. *Science*, 335(6069), 705–708. <https://doi.org/10.1126/science.1215141>
- Klein, E., Duputel, Z., Zigone, D., Vigny, C., Boy, J.-P., Doubre, C., & Meneses, G. (2018). Deep transient slow slip detected by survey GPS in the region of Atacama, Chile. *Geophysical Research Letters*, 45(22), 12263–12273. <https://doi.org/10.1029/2018GL080613>
- Klein, E., Potin, B., Pasten-Araya, F., Tissandier, R., Azua, K., Duputel, Z., et al. (2021). Interplay of seismic and a-seismic deformation during the 2020 sequence of Atacama, Chile. *Earth and Planetary Science Letters*, 570, 117081. <https://doi.org/10.1016/j.epsl.2021.117081>
- Klein, E., Vigny, C., Duputel, Z., Zigone, D., Rivera, L., Ruiz, S., & Potin, B. (2023). Return of the Atacama deep slow slip event: The 5-year recurrence confirmed by continuous GPS. *Physics of the Earth and Planetary Interiors*, 334, 106970. <https://doi.org/10.1016/j.pepi.2022.106970>
- Larson, K. M., Bilich, A., & Axelrad, P. (2007). Improving the precision of high-rate GPS. *Journal of Geophysical Research*, 112(B5), B05422. <https://doi.org/10.1029/2006JB004367>
- Latour, S., Schubnel, A., Nielsen, S., Madariaga, R., & Vinciguerra, S. (2013). Characterization of nucleation during laboratory earthquakes. *Geophysical Research Letters*, 40(19), 5064–5069. <https://doi.org/10.1002/grl.50974>
- Llenos, A. L., McGuire, J. J., & Ogata, Y. (2009). Modeling seismic swarms triggered by aseismic transients. *Earth and Planetary Science Letters*, 281(1), 59–69. <https://doi.org/10.1016/j.epsl.2009.02.011>
- Lohman, R. B., & McGuire, J. J. (2007). Earthquake swarms driven by aseismic creep in the Salton Trough, California. *Journal of Geophysical Research*, 112(B4), B04405. <https://doi.org/10.1029/2006JB004596>
- Lomax, A. (2017). NonLinLoc 7.0 [software]. NonLinLoc. Retrieved from <http://alomax.free.fr/nlloc/>
- Lomax, A., Virieux, J., Volant, P., & Berge-Thierry, C. (2000). Probabilistic earthquake location in 3D and layered models. In G. Nolet, C. H. Thurber, & N. Rabinowitz (Eds.), *Advances in seismic event location* (Vol. 18, pp. 101–134). https://doi.org/10.1007/978-94-015-9536-0_5
- Marill, L., Marsan, D., Socquet, A., Radiguet, M., Cotte, N., & Rousset, B. (2021). Fourteen-year acceleration along the Japan Trench. *Journal of Geophysical Research: Solid Earth*, 126(11), e2020JB021226. <https://doi.org/10.1029/2020JB021226>
- Marone, C. J., Scholtz, C. H., & Bilham, R. (1991). On the mechanics of earthquake afterslip. *Journal of Geophysical Research*, 96(B5), 8441–8452. <https://doi.org/10.1029/91JB00275>
- Marsan, D., & Enescu, B. (2012). Modeling the foreshock sequence prior to the 2011, Mw 9.0 Tohoku, Japan, earthquake. *Journal of Geophysical Research*, 117(B6), B06316. <https://doi.org/10.1029/2011JB009039>
- Marsan, D., Helmstetter, A., Bouchon, M., & Dublanche, P. (2014). Foreshock activity related to enhanced aftershock production: Foreshock and aftershock activities. *Geophysical Research Letters*, 41(19), 6652–6658. <https://doi.org/10.1002/2014GL061219>
- Marsan, D., & Lengliné, O. (2008). Extending earthquakes' reach through cascading. *Science*, 319(5866), 1076–1079. <https://doi.org/10.1126/science.1148783>
- Marsan, D., & Lengliné, O. (2010). A new estimation of the decay of aftershock density with distance to the mainshock. *Journal of Geophysical Research*, 115(B9), B09302. <https://doi.org/10.1029/2009jb007119>
- Mavrommatis, A. P., Segall, P., & Johnson, K. M. (2014). A decadal-scale deformation transient prior to the 2011 Mw 9.0 Tohoku-Oki earthquake. *Geophysical Research Letters*, 41(13), 4486–4494. <https://doi.org/10.1002/2014GL060139>
- Mavrommatis, A. P., Segall, P., Uchida, N., & Johnson, K. M. (2015). Long-term acceleration of aseismic slip preceding the Mw 9 Tohoku-Oki earthquake: Constraints from repeating earthquakes. *Geophysical Research Letters*, 42(22), 9717–9725. <https://doi.org/10.1002/2015GL066609>
- McLaskey, G. C. (2019). Earthquake initiation from laboratory observations and implications for foreshocks. *Journal of Geophysical Research: Solid Earth*, 124(12), 12882–12904. <https://doi.org/10.1029/2019JB018363>
- Meng, Q., & Duan, B. (2022). Dynamic modeling of interactions between shallow slow-slip events and subduction earthquakes. *Seismological Research Letters*, 94(1), 206–216. <https://doi.org/10.1785/0220220138>
- Mignan, A. (2015). The debate on the prognostic value of earthquake foreshocks: A meta-analysis. *Scientific Reports*, 4(1), 4099. <https://doi.org/10.1038/srep04099>
- Miura, S., Iinuma, T., Yui, S., Uchida, N., Sato, T., Tachibana, K., & Hasegawa, A. (2006). Co- and post-seismic slip associated with the 2005 Miyagi-Oki earthquake (m7.2) as inferred from GPS data. *Earth Planets and Space*, 58(12), 1567–1572. <https://doi.org/10.1186/BF0352662>
- Mousavi, S. M., Ellsworth, W. L., Zhu, W., Chuang, L. Y., & Beroza, G. C. (2020a). Earthquake transformer—An attentive deep-learning model for simultaneous earthquake detection and phase picking. *Nature Communications*, 11(1), 3952. <https://doi.org/10.1038/s41467-020-17591-w>
- Mousavi, S. M., Ellsworth, W. L., Zhu, W., Chuang, L. Y., & Beroza, G. C. (2020b). EQTransformer [software]. GitHub. Retrieved from <https://github.com/smousavi05/EQTransformer>
- Moutote, L., Lengliné, O., & Duputel, Z. (2023). ValEqt: A high-resolution earthquake and repeating earthquakes catalog of the 2017 Valparaiso sequence [Dataset]. Zenodo. <https://doi.org/10.5281/zenodo.7665026>
- Moutote, L., Marsan, D., Lengliné, O., & Duputel, Z. (2021). Rare occurrences of non-cascading foreshock activity in Southern California. *Geophysical Research Letters*, 48(7), e2020GL091757. <https://doi.org/10.1029/2020GL091757>

- Nadeau, R. M., & Johnson, L. R. (1998). Seismological studies at Parkfield VI: Moment release rates and estimates of source parameters for small repeating earthquakes. *Bulletin of the Seismological Society of America*, 88(3), 790–814. <https://doi.org/10.1785/BSSA0880030790>
- Nishikawa, T., Nishimura, T., & Okada, Y. (2021). Earthquake swarm detection along the Hikurangi Trench, New Zealand: Insights into the relationship between seismicity and slow slip events. *Journal of Geophysical Research: Solid Earth*, 126(4), e2020JB020618. <https://doi.org/10.1029/2020JB020618>
- Ogata, Y. (1988). Statistical models for earthquake occurrences and residual analysis for point processes. *Journal of the American Statistical Association*, 83(401), 9–27. <https://doi.org/10.1080/01621459.1988.10478560>
- Ogata, Y. (1989). Statistical model for standard seismicity and detection of anomalies by residual analysis. *Tectonophysics*, 169(1–3), 159–174. [https://doi.org/10.1016/0040-1951\(89\)90191-1](https://doi.org/10.1016/0040-1951(89)90191-1)
- Ogata, Y. (1992). Detection of precursory relative quiescence before great earthquakes through a statistical model. *Journal of Geophysical Research*, 97(B13), 19845. <https://doi.org/10.1029/92JB00708>
- Ohnaka, M. (1992). Earthquake source nucleation: A physical model for short-term precursors. *Tectonophysics*, 211(1), 149–178. [https://doi.org/10.1016/0040-1951\(92\)90057-D](https://doi.org/10.1016/0040-1951(92)90057-D)
- Omori, F. (1895). On the after-shocks of earthquakes. *The Journal of the College of Science, Imperial University*, 7(2), 111–200. <https://doi.org/10.15083/00037562>
- Pedregosa, F., Varoquaux, G., Gramfort, A., Michel, V., Thirion, B., Grisel, O., et al. (2011). Scikit-learn: Machine learning in python. *Journal of Machine Learning Research*, 12, 2825–2830.
- Peng, Z., Vidale, J. E., Ishii, M., & Helmstetter, A. (2007). Seismicity rate immediately before and after main shock rupture from high-frequency waveforms in Japan. *Journal of Geophysical Research*, 112(B3), B03306. <https://doi.org/10.1029/2006jb004386>
- Perfettini, H., & Avouac, J.-P. (2007). Modeling afterslip and aftershocks following the 1992 landers earthquake. *Journal of Geophysical Research*, 112(B7), B07409. <https://doi.org/10.1029/2006JB004399>
- Perfettini, H., Frank, W. B., Marsan, D., & Bouchon, M. (2018). A model of aftershock migration driven by afterslip. *Geophysical Research Letters*, 45(5), 2283–2293. <https://doi.org/10.1002/2017GL076287>
- Periollat, A., Radiguet, M., Weiss, J., Twardzik, C., Amitrano, D., Cotte, N., et al. (2022). Transient brittle creep mechanism explains early post-seismic phase of the 2011 Tohoku-Oki megathrust earthquake: Observations by high-rate GPS solutions. *Journal of Geophysical Research: Solid Earth*, 127(8), e2022JB024005. <https://doi.org/10.1029/2022JB024005>
- Radiguet, M., Cotton, F., Vergnolle, M., Campillo, M., Walpersdorf, A., Cotte, N., & Kostoglodov, V. (2012). Slow slip events and strain accumulation in the Guerrero gap, Mexico. *Journal of Geophysical Research*, 117(B4), B04305. <https://doi.org/10.1029/2011JB008801>
- Radiguet, M., Perfettini, H., Cotte, N., Gualandi, A., Valette, B., Kostoglodov, V., et al. (2016). Triggering of the 2014 Mw7.3 Papanoa earthquake by a slow slip event in Guerrero, Mexico. *Nature Geoscience*, 9(11), 829–833. <https://doi.org/10.1038/ngeo2817>
- Ragheb, A., Clarke, P. J., & Edwards, S. (2007). GPS sidereal filtering: Coordinate-and carrier-phase-level strategies. *Journal of Geodesy*, 81(5), 325–335. <https://doi.org/10.1007/s00190-006-0113-1>
- Richter, C. F. (1935). An instrumental earthquake magnitude scale. *Bulletin of the Seismological Society of America*, 25(1), 2–32. <https://doi.org/10.1785/BSSA0250010001>
- Richter, C. F. (1958). Elementary seismology.
- Rogers, G., & Dragert, H. (2003). Episodic tremor and slip on the cascadia subduction zone: The chatter of silent slip. *Science*, 300(5627), 1942–1943. <https://doi.org/10.1126/science.1084783>
- Ross, Z. E., Trugman, D. T., Hauksson, E., & Shearer, P. M. (2019). Searching for hidden earthquakes in Southern California. *Science*, 364(6442), 767–771. <https://doi.org/10.1126/science.aaw6888>
- Rubin, A. M., & Ampuero, J.-P. (2005). Earthquake nucleation on (aging) rate and state faults. *Journal of Geophysical Research*, 110(B11), B11312. <https://doi.org/10.1029/2005JB003686>
- Ruiz, S., Aden-Antoniow, F., Baez, J. C., Otarola, C., Potin, B., del Campo, F., et al. (2017). Nucleation phase and dynamic inversion of the Mw 6.9 Valparaíso 2017 earthquake in Central Chile. *Geophysical Research Letters*, 44(20), 10290–10297. <https://doi.org/10.1002/2017GL075675>
- Ruiz, S., Metois, M., Fuenzalida, A., Ruiz, J., Leyton, F., Grandin, R., et al. (2014). Intense foreshocks and a slow slip event preceded the 2014 Iquique Mw 8.1 earthquake. *Science*, 345(6201), 1165–1169. <https://doi.org/10.1126/science.1256074>
- Seif, S., Zechar, J. D., Mignan, A., Nandan, S., & Wiemer, S. (2019). Foreshocks and their potential deviation from general seismicity. *Bulletin of the Seismological Society of America*, 109(1), 1–18. <https://doi.org/10.1785/0120170188>
- Shearer, P. M. (2019). In *Introduction to Seismology* (3rd ed. ed.).
- Socquet, A., Valdes, J. P., Jara, J., Cotton, F., Walpersdorf, A., Cotte, N., et al. (2017). An 8 month slow slip event triggers progressive nucleation of the 2014 Chile Megathrust. *Geophysical Research Letters*, 44(9), 4046–4053. <https://doi.org/10.1002/2017GL073023>
- Sun, T., & Wang, K. (2015). Viscoelastic relaxation following subduction earthquakes and its effects on afterslip determination. *Journal of Geophysical Research: Solid Earth*, 120(2), 1329–1344. <https://doi.org/10.1002/2014jb011707>
- Tape, C., Holtkamp, S., Silwal, V., Hawthorne, J., Kaneko, Y., Ampuero, J. P., et al. (2018). Earthquake nucleation and fault slip complexity in the lower crust of central Alaska. *Nature Geoscience*, 11(7), 536–541. <https://doi.org/10.1038/s41561-018-0144-2>
- Taroni, M., Marzocchi, W., Schorlemmer, D., Werner, M. J., Wiemer, S., Zechar, J. D., et al. (2018). Prospective CSEP evaluation of 1-day, 3-month, and 5-yr earthquake forecasts for Italy. *Seismological Research Letters*, 89(4), 1251–1261. <https://doi.org/10.1785/0220180031>
- Uchida, N. (2019). Detection of repeating earthquakes and their application in characterizing slow fault slip. *Progress in Earth and Planetary Science*, 6(1), 40. <https://doi.org/10.1186/s40645-019-0284-z>
- Utsu, T., Ogata, Y., S. R., & Matsu'ura (1995). The centenary of the Omori formula for a decay law of aftershock activity. *Journal of Physics of the Earth*, 43(1), 1–33. <https://doi.org/10.4294/jpe1952.43.1>
- Vallée, M., Nocquet, J.-M., Battaglia, J., Font, Y., Segovia, M., Régnier, M., et al. (2013). Intense interface seismicity triggered by a shallow slow slip event in the Central Ecuador subduction zone. *Journal of Geophysical Research: Solid Earth*, 118(6), 2965–2981. <https://doi.org/10.1002/jgrb.50216>
- van den Ende, M. P. A., & Ampuero, J.-P. (2020). On the statistical significance of foreshock sequences in Southern California. *Geophysical Research Letters*, 47(3), e2019GL086224. <https://doi.org/10.1029/2019GL086224>
- Voss, N., Dixon, T. H., Liu, Z., Malservisi, R., Protti, M., & Schwartz, S. (2018). Do slow slip events trigger large and great megathrust earthquakes? *Science Advances*, 4(10), eaat8472. <https://doi.org/10.1126/sciadv.aat8472>
- Waldhauser, F., & Ellsworth, W. L. (2000). A double-difference earthquake location algorithm: Method and application to the Northern Hayward Fault, California. *Bulletin of the Seismological Society of America*, 90(6), 1353–1368. <https://doi.org/10.1785/0120000006>
- Waldhauser, F., & Ellsworth, W. L. (2010). HypoDD 1.3 [Dataset]. Lamont-Doherty Earth Observatory. Retrieved from <https://www.ldeo.columbia.edu/~felixw/hypoDD.html>

- Wang, K., Hu, Y., & He, J. (2012). Deformation cycles of subduction earthquakes in a viscoelastic Earth. *Nature*, *484*(7394), 327–332. <https://doi.org/10.1038/nature11032>
- Wdowinski, S., Bock, Y., Zhang, J., Fang, P., & Genrich, J. (1997). Southern California permanent GPS geodetic array: Spatial filtering of daily positions for estimating coseismic and postseismic displacements induced by the 1992 landers earthquake. *Journal of Geophysical Research*, *102*(B8), 18057–18070. <https://doi.org/10.1029/97JB01378>
- Zhang, M., Ellsworth, W. L., & Beroza, G. C. (2019a). Rapid earthquake association and location. *Seismological Research Letters*, *90*(6), 2276–2284. <https://doi.org/10.1785/0220190052>
- Zhang, M., Ellsworth, W. L., & Beroza, G. C. (2019b). REAL [Software]. GitHub. Retrieved from <https://github.com/Dal-mzhang/REAL>
- Zhuang, J. (2012). Long-term earthquake forecasts based on the epidemic-type aftershock sequence (ETAS) model for short-term clustering. *Research in Geophysics*, *2*(1), e8. <https://doi.org/10.4081/rg.2012.e8>
- Zhuang, J., Harte, D., Werner, M. J., Hainzl, S., & Zhou, S. (2012). *Basic models of seismicity: Temporal models*. Community Online Resource for Statistical Seismicity Analysis, Theme V (1).
- Zhuang, J., & Touati, S. (2015). *Stochastic simulation of earthquake catalogs* (p. 34). Community Online Resource for Statistical Seismicity Analysis, Theme V (1).
- Zhuang, J., Werner, M. J., Hainzl, S., Harte, D., & Zhou, S. (2011). *Basic models of seismicity: Spatiotemporal models* (p. 20). Community Online Resource for Statistical Seismicity Analysis, Theme V (1).